Fall 2014

Experimental Characterization Of Cu Free-Air Ball And Simulations Of Dielectric Fracture During Wire Bonding

Sai Sudharsanan Paranjothy
Purdue University

Graduate School Form 30
(Updated 11/20/2014)

PURDUE UNIVERSITY
GRADUATE SCHOOL
Thesis/Dissertation Acceptance

This is to certify that the thesis/dissertation prepared

By Sai Sudharsanan Paranjothy

Entitled
EXPERIMENTAL CHARACTERIZATION OF CU FREE-AIR BALL AND SIMULATIONS OF DIELECTRIC FRACTURE DURING WIRE BONDING

For the degree of Master of Science in Mechanical Engineering

Is approved by the final examining committee:

Ganesh Subbarayan

Ghadir Haikal

Marcial Gonzalez

To the best of my knowledge and as understood by the student in the Thesis/Dissertation Agreement, Publication Delay, and Certification/Disclaimer (Graduate School Form 32), this thesis/dissertation adheres to the provisions of Purdue University's "Policy on Integrity in Research" and the use of copyrighted material.

Ganesh Subbarayan

Approved by Major Professor(s): _____

_____

Approved by: Ganesh Subbarayan 12/08/2014

Head of the Department Graduate Program Date

EXPERIMENTAL CHARACTERIZATION OF CU FREE-AIR BALL AND SIMULATIONS OF DIELECTRIC FRACTURE DURING WIRE BONDING

A Thesis

Submitted to the Faculty

of

Purdue University

by

Sai Sudharsanan Paranjothy

In Partial Fulfillment of the

Requirements for the Degree

of

Master of Science in Mechanical Engineering

December 2014

Purdue University

West Lafayette, Indiana

Dedicated to the man who sacrificed even his sleep for the dreams of his sons

My father, Paranjothy Thankiah

And to the woman who made many such sacrifices possible

My mother, Shanthi Paranjothy

ACKNOWLEDGEMENTS

I forever am obliged to each and every individual who has been a part of this wonderful journey at Purdue University for the past couple of years. I am ever indebted to Professor Ganesh Subbarayan for his guidance through my course of study. I consider it a privilege to have been a part of his research group, and have been a fond admirer of his depth of knowledge, insight, and ability to explain a multitude of phenomena with a fundamental concept. I am fortunate to have been inspired by his methods of reasoning and his attention to detail. It is truly a wonderful opportunity to have a mentor who genuinely cares about the betterment of his students in every aspect of their life. I would like to thank him for his intellectual resources, laboratory facilities, and the opportunities to participate in conferences and be a part of a larger scientific community. I am certain that I would fondly recollect our research group meetings, when discussions sometimes led to a "passionate debate" between Professor and Subramanya. I am bound to miss these wonderful days.

I would like to thank Prof. Marcial Gonzalez and Prof. Ghadir Haikal for being a part of my advisory committee.

I am thankful to each and every research group member, Kritika, Anirudh, Yuvraj, Hung-Yun, Subramanya, Tao, Mesut, Yiran and Chun-pei. I would also like to thank former group members to whose work I have referred, Dennis, Abhishek, Allen and Dhruv. I specifically am more thankful to Yuvraj, for his help in constructing the experimental apparatus, Hung-Yun for his finite element model on wire bonding and Kritika for her guidance on using the isogeometric tool.

I am thankful to Semiconductor Research Corporation for making this study possible under SRC Task id 1292.075, Freescale Semiconductor for their support with free-air ball samples and SIMULIA for the computational resources.

At this juncture, I also am completing my six month stint at SIMULIA, Dassault Systèmes, as an intern. I am thankful to Mr.Steve Crowley for recruiting me at West Lafayette office, where I had the wonderful chance to work under Mr. Bob Durbin's guidance. I am thankful to each and every person at SIMULIA to have been a part of my wonderful experience and learning opportunity. Specifically, I would like to thank Min, Srinivas, Ryan Beckett, Dipesh and Dr.Mao for their guidance and patience in answering many of my inexperienced questions. My special thanks to Elizabeth for her friendship.

I am thankful to Ryan Christopher Jones, my supervisor at Sagamore Restaurant at Purdue, without whom my first year of sustenance in a new country might have been very difficult. I am ever indebted to his kindness in employing me, and it is not an exaggeration to say that it is one of my fondest memories, waiting tables with fellow 'Sagamorians'.

I would like to thank my friends from high school, College of Engineering Guindy and Larsen and Toubro Ltd to have always maintained a closeness though miles apart, making me survive turbulent days. Thanks to my house mates, Rubin and Sid, who have kindly tolerated my quirks and heated metaphysical arguments on Friday evenings.

Before all, none of this would have been possible if not for the hard work and support of my father, Mr.T. Paranjothy and mother, Mrs. P.Shanthi. I am ever indebted to them for every step in my life and every accomplishment.

At last, I would also sincerely thank some who have undermined me, lied and betrayed me in some regard, from which I usually derive a tremendous motivation to succeed, towards which I consider this as my first step.

TABLE OF CONTENTS

Page

Page

LIST OF TABLES

LIST OF FIGURES

Figure Page

Figure Page

Figure Page

ABSTRACT

Paranjothy, Sai Sudharsanan. M.S.M.E., Purdue University, December 2014. Experimental Characterization of Cu Free-Air Ball and Simulations of Dielectric Fracture during Wire Bonding. Major Professor: Ganesh Subbarayan, School of Mechanical Engineering

Wire bonding is the process of forming electrical connection between the integrated circuit (IC) and its structural package. ICs made of material with low dielectric constant (low-k) and ultra low-k are porous in nature, and are prone to fracture induced failure during packaging process. In recent years, there is increasing interest in copper wire bond technology as an alternative to gold wire bond in microelectronic devices due to its superior electrical performance and low cost. Copper wires are also approximately 25% more conductive than Au wires aiding in better heat dissipation. At present, validated constitutive models for the strain rate and temperature dependent behavior of Cu free-air ball (FAB) appear to be largely missing in the literature. The lack of reliable constitutive models for the Cu FAB has hampered the modeling of the wire bonding process and the ability to assess risk of fracture in ultra low-k dielectric stacks. The challenge to FAB characterization is primarily due to the difficulty in performing mechanical tests on spherical FAB of micrometers in size. To address this challenge, compression tests are performed on FAB using custom-built microscale tester in the current study. Specifically, the tester has three closed-loop controlled linear stages with submicron resolution, a manual tilt stage, a six-axis load cell with sub-Newton load resolution for eliminating misalignment, a milliNewton resolution load cell for compression load measurement, a capacitance sensor to estimate sample deformation and to control the vertical stage in closed loop, a high working depth camera for viewing the sample deformation, and controllers for the stages implemented in the LabVIEW environment. FAB is compressed between tungsten carbide punches and a constitutive model is developed for Cu FAB

through an inverse modeling procedure. In the inverse procedure, appropriate constitutive model parameter values are iterated through an automated optimization workflow, until the load-displacement response matches the experimentally observed response. Using the material properties obtained from the experiment, a “macroscale” finite element model for the impact and ulatrasonic vibration stages of wire bonding process is constructed to simulate (a) Plastic deformation of the Cu FAB at different time steps (b) Evolution of contact pressure (c) Phenomenon such as pad splash and lift-off. The deformations from the macroscale model are provided as input to a microscale model of the dielectric with copper vias as well as line-type heterogeneities. The microscale model is used to identify potential crack nucleation sites as well as the crack path within the ILD stack during wire bonding. The modeling provides insight into the relative amounts of damage accumulated during the impact and the ultrasonic excitation stages.

In general, Bonding over Active Circuit (BOAC) has made wire bonding a considerable challenge due to the brittleness of the dielectric. Identifying and locating microscale fractures beneath the bond pads during wire bonding require extensive sample preparation and investigation for microscopic characterization. While simulations of fracture are an attractive alternative to trial and error microscopic characterization, the length scale of components involved in wire bonding varies from millimeters to nanometers. Therefore, constructing a finite element mesh across the model is computationally costly. Also, a multi-scale simulation framework is necessary. Such a modeling framework is also developed in this work to predict crack nucleation and propagation in wire bond induced failure.

CHAPTER 1. INTRODUCTION

1.1 Wire Bonding

Electronic packaging refers to the process of enclosing electronic components in a protective framework that prevents them from damage. The packaging not only acts as a structural framework that allows the ICs to be integrated into a single assembly, but could also play a role in forming electrical connection between individual electronic components.

After the silicon wafer is fabricated, it is diced into individual chips or dies using a diamond saw. The IC chip is then mounted on to a substrate using a suitable die attach material and is then cured. Then follows wire bonding [1,2], the process of forming an electrical connection between the die and the metallic lead frame of the electronic package. An IC along with its package is shown in Figure 1-1

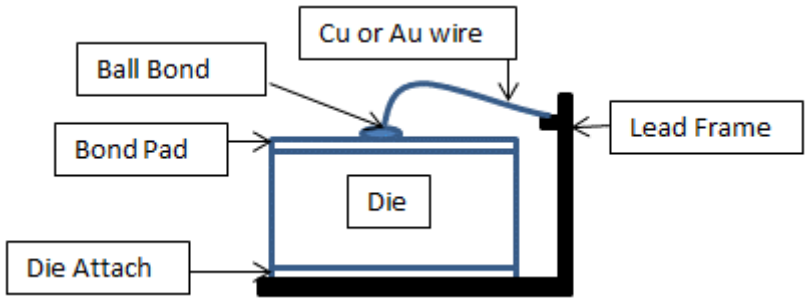

Figure 1-1. Schematic representation of an IC wire bonded to the package.

Approximately 87% [3] of the connections in micro-electronic devices are realized by wire bonding. To form such a connection, a wire typically made of gold is first bonded on

to the bond pad and then to lead finger on the packaging side. Wire bonding consists of two stages:

- Thermosonic ball bonding
- Ultrasonic wedge bonding

In thermosonic ball bonding, high pressure, high temperature and vibration energy are used to accomplish wire bonding. An ultrasonic wedge bonding is carried out at room temperature with high ultrasonic energy and pressure. A step wise outline of the ball bonding process follows [4] :

(i) An unprocessed wire is threaded through the capillary and the length of the unprocessed wire beneath the capillary determines the size of the Free-Air Ball (FAB).

(ii) A very high voltage is discharged through electrodes, thereby melting the wire and forming the FAB. This is the process of 'electronic flame-off'.

(iii) Formation of the first bond occurs by the downward motion of the capillary. The FAB is collapsed on the pad with a vertical impact force and then is bonded to the pad using an ultrasonic vibration for a period of time. The bonding occurs due to formation of interface between the wire material and the bond pad (Figure 1-4), mainly due to the plastic deformation and slip between the two materials. There is a risk of fracture of the underlying dielectrics during this process.

(iv) The Capillary then raises, forms a loop and then descends on to the substrate, completing the second bond on the substrate. The wire is cut off and the process is then repeated in cycles.

As the devices and dies get smaller, economizing the space between the bonds on the pads becomes important. The bond pad pitch (BPP) has shrunk to a mere 35 μm in ultra-fine pitch wire bonding. In order to achieve a finer wire pitch, a thorough understanding of the materials involved in the process is necessary.

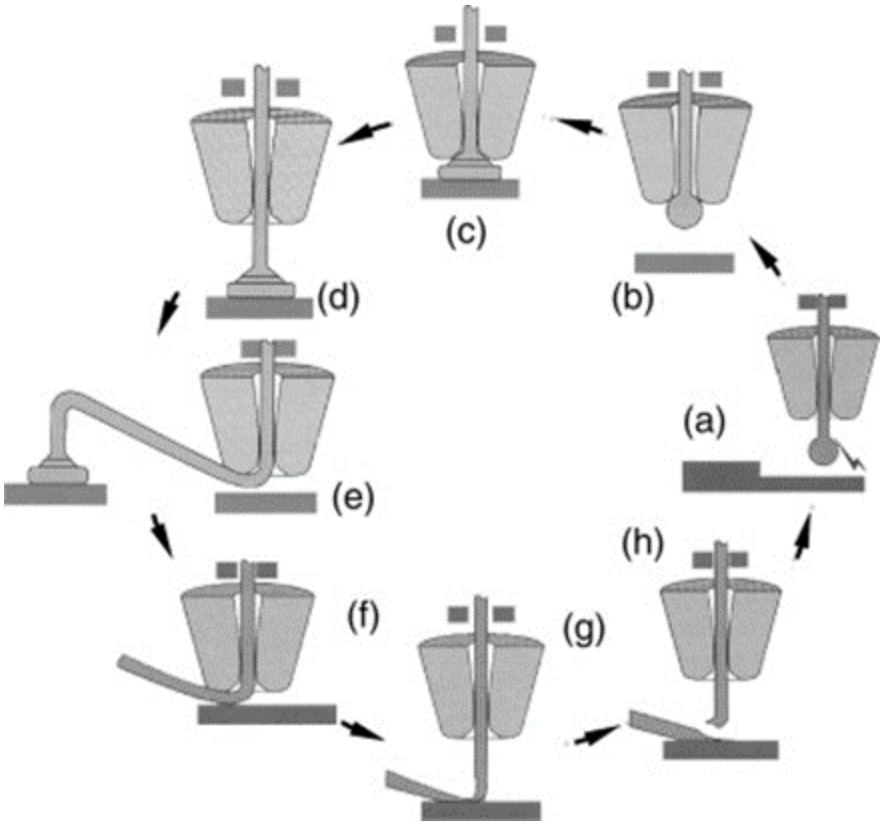

Figure 1-2. (a) Wire is threaded through capillary and FAB is formed through electronic flame-off (b) FAB is positioned above bond pad and downward motion of the capillary begins (c) Formation of the first bond on pad (d) Capillary rises (e) Loop formation (f) Positioning over the lead frame (g) wedge bond formation on the lead frame (g) Wire tail is formed and the cycle repeats [5].

1.2 Materials in Wire Bonding

Some of the desired qualities of the material of the wire in bonding process are high electrical conductivity, high tensile strength, malleability and high current carrying capability, to name a few. A 99.99% pure Au is a popular material of choice because of high electrical conductivity, low corrosiveness, and high strength [4]. Aluminum may also serve as a potential bonding material, but due to the complexity of equipment and tooling required to perform Al ball boding under ambient conditions, it is not used currently. However, due to better thermal and electrical conductivity, mechanical properties and cost, Cu is gradually replacing Au in wire bonding. Cu also possesses

higher mechanical strength [6]. Properties of Au, Al and Cu are presented in comparison through the Table 1-1 and Figure 1-1 that follow.

Table 1-1. Comparison of Au, Cu and Al properties [7].

Property	Units	Gold	Copper	Aluminum
Melting Point	°C	1063	1083	660
Specific Heat (20°C)	J/mol-K	25.4	24.4	24.2
Heat of Fusion	KJ/mol	12.55	13.05	10.71
Thermal Conductivity	W/m-K	311	394	222
Electrical Resistance	10^{-8} Ohm-m	2.2	1.7	2.8
CTE	ppm/K	14.2	16.5	23.1

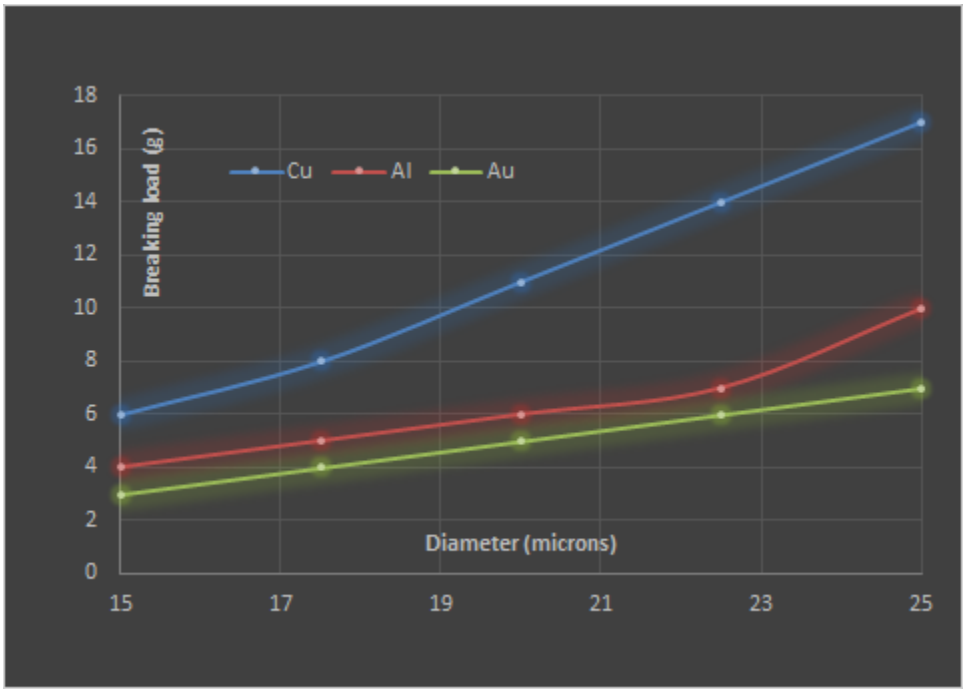

Figure 1-3. Comparison of breaking load between Cu, Al and Au wires of different diameters, adopted from [8].

From Table 1-1 [7], it can be observed that Cu has 25% higher thermal conductivity and 30% lower resistance than Au. In terms of ultimate tensile strength, it is 40% percent better than Au, and thus requires higher force for bonding on to the bond pad. Higher bond force in turn increases the risk of fracture in the underlying dielectric layers.

1.3 Risk of Fracture in Interlayer Dielectric

Interlayer Dielectric (ILD) fracture is the phenomenon where circuit failure occurs due to the damage of the underlying dielectric, and is an important reliability consideration. Material with low dielectric constant, referred to as low-k and ultra low-k (ULK) dielectric are expected to remain in gold or copper wire bonded packages [9]. There is a need to place bond pads over active circuitry which is a significant reliability challenge in low-k and ULK dies [10].

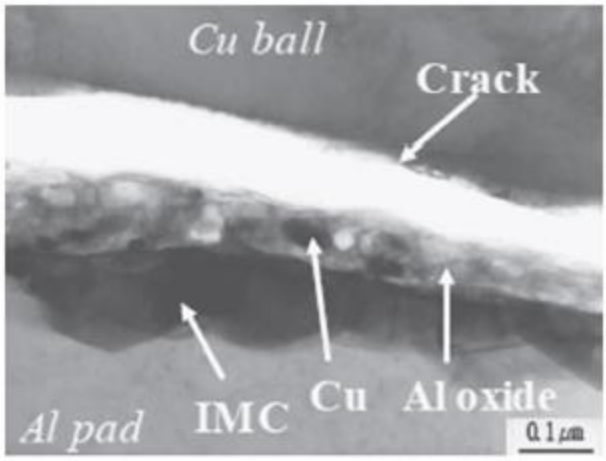

Figure 1-4. Cu bond formation over Al pad shown along with intermetallic compound formation and crack [11].

The main issue with ILD cracking is that it might not be possible to detect it through visual inspection, since it mostly occurs beneath the bond pad and is only deduced during reliability testing. Though many factors can be attributed to cracking and influence each other in complicated and adverse manner, bonding impact force, ultrasonic excitation energy, temperature of the bonding process and the material of the underlying dielectric

play an important role. The bonding temperature might reach up to 250 °C and such temperatures further degrade the mechanical properties of the materials involved. Since Cu is stiffer than Au, it requires higher bonding force and ultrasonic excitation for bonding. Thus, the risks of ILD cracking are higher in Cu wire bonding process.

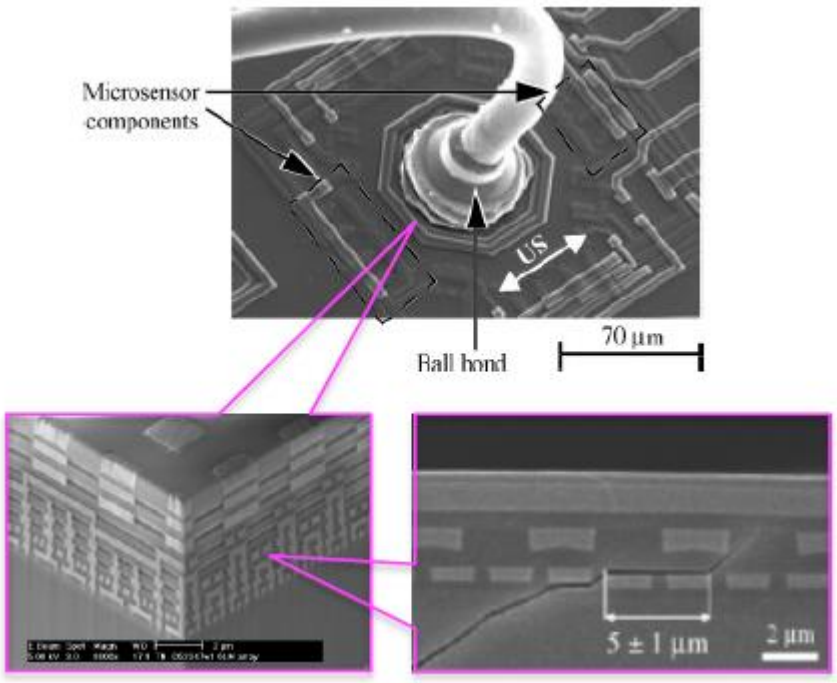

Figure 1-5. Interlayer dielectric fracture due to wire bonding. Shown are the stacks with active circuit , which are few micrometers in scale [12].

1.4 Need for Cu FAB Characterization

FAB are formed by the process of 'Electronic Flame-off' (EFO), where an electrical discharge is used to melt the tip of the unprocessed wire into spherical shape. Due to recrystallization that occurs during the process, the properties of the FAB are significantly different and are softer than the Cu wire [13]. Thus, data from tensile tests performed on the unprocessed wire are not suitable to form constitutive models to represent the behavior of the FAB.

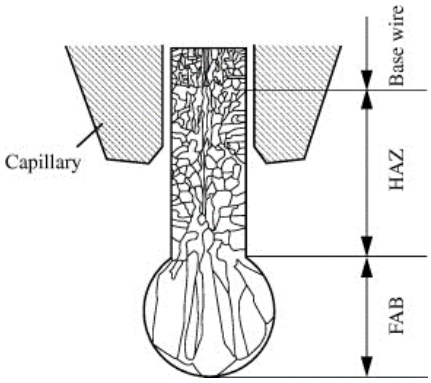

Figure 1-6. Grain reorientation due to electronic flame-off [14].

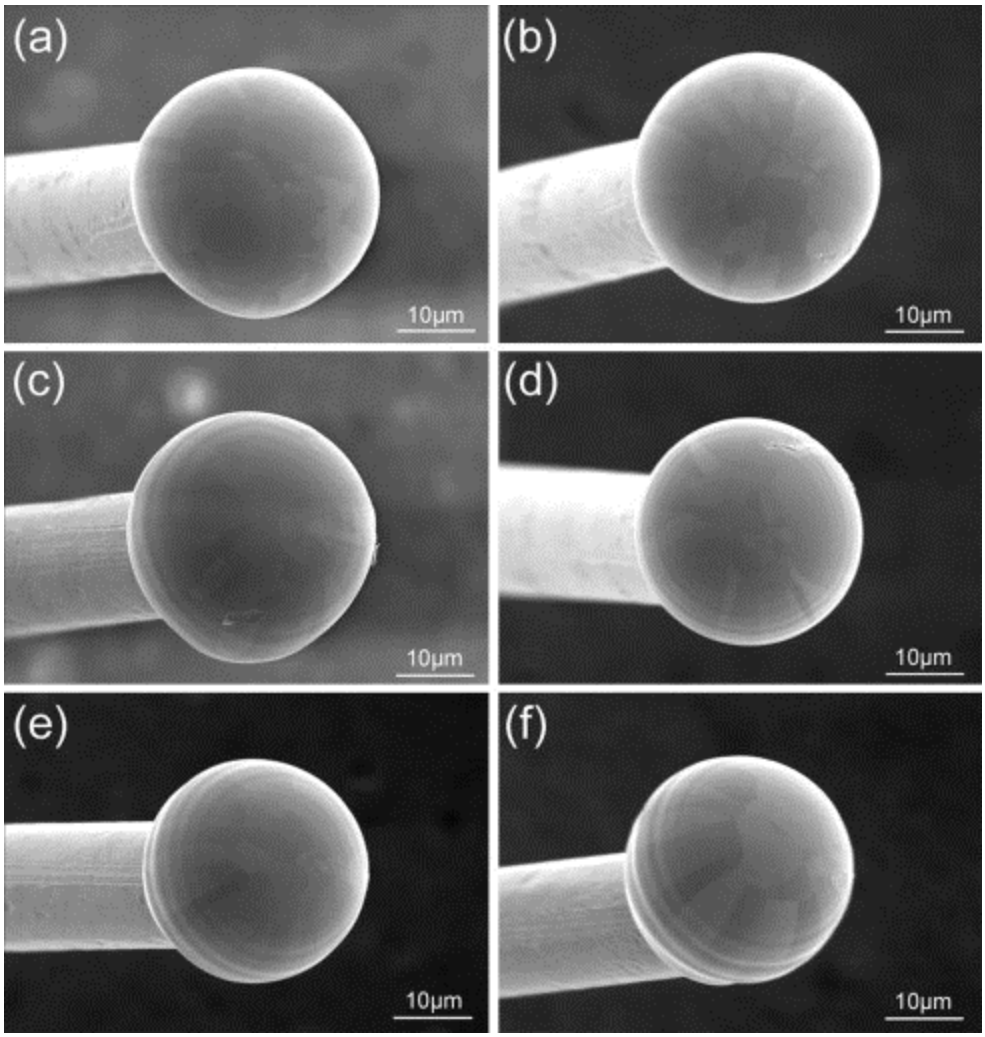

Figure 1-7. Grain orientation study at 1.2 mil under different EFO currents [15] (a) 20 mA; (b) 22 mA; (c) 30 mA; (d) 40 mA; (e) 50 mA and (f) 60 mA.

Though studies exist relating the parameters of EFO to the shape and size of FAB [15], validated constitutive models for behavior of Cu FAB appear to be largely missing in the literature, save for reference [13]. But, this study does not provide the temperature and strain-rate dependent behavior of Cu FAB, which are important taking into consideration the high rate, high temperature environment during the wire bonding process. The lack of reliable constitutive models for the Cu FAB has hampered the modeling of the wire bonding process and the ability to assess risk of fracture in ULK dielectric stacks. Thus, experimental characterization of Cu FAB is necessary to extract temperature and rate dependent constitutive model parameters.

1.5 Challenges in Experimental Characterization of FAB

Although nano-indentation tests are common for micron scale objects such as the FAB, the hardness values are by themselves of relatively little use in modeling wire bonding process or in assessing the risk of fracture in chip dielectric stacks. There are two main difficulties in characterizing the FAB. The first is related to its spherical shape which makes it difficult to obtain stress-strain behavior directly from standard compression tests. The second is the microscale diameter, which necessitates the construction of a custom-microtester, combining equipment with capabilities of interest.

1.6 Research Objective

In this work, the experimental characterization of Cu FAB, 25 microns in diameter is presented at low and intermediate strain rates ($0.001s^{-1}$-$4s^{-1}$). A custom microscale tester was constructed to enable the testing of the FAB under low and intermediate strain rate conditions. Specifically, the tester has three linear stages with submicron resolutions, a manual tilt stage, a six-axis load cell with sub-Newton load resolution for eliminating misalignment, a milliNewton resolution single-axis load cell, a capacitance sensor to estimate sample deformation and to control the vertical stage in closed loop, a high working depth lens for viewing the sample deformation, and controllers for the stages implemented in the LabVIEW environment [16]. The FAB is compressed between tungsten carbide punches and constitutive models are developed for the copper FAB

through an inverse modeling procedure. In the inverse procedure, the constitutive model parameter values are iterated using an automated optimization procedure, until the finite element load-displacement response matches the experimentally observed response.

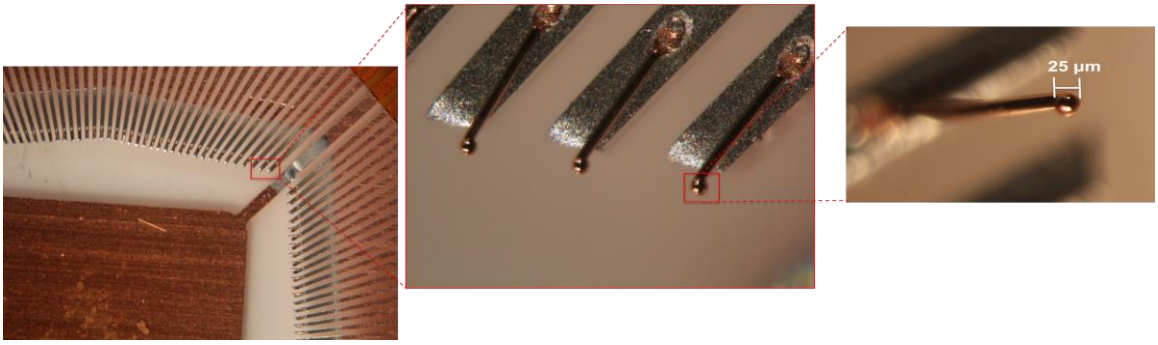

Figure 1-8. 25 µm FAB attached to the lead frame.

Elastic and elasto-plastic contact theories such as Hertz model, Tatara model and Thornton model are applied to understand the force-displacement (P-δ) behavior. An analytic approach is then enforced to derive the strain-hardening index using a Ramberg-Osgood type stress-strain relationship in the contact theories. To have 'unified' constitutive model parameters to explain the behavior at all strain rates and temperature, viscoplastic constitutive model (Anand's Model) parameters are obtained through inverse finite element modeling. The model parameters are iterated through an optimization algorithm until the obtained P-δ response matches with the experimental response obtained at both low and intermediate strain rates. A “macroscale” finite element model for the impact and ultrasonic vibration stages of wire bonding process was constructed to simulate the plastic deformation of the Cu FAB at different time steps and study the evolution of contact pressure, deformation of the FAB and other parameters of interest.

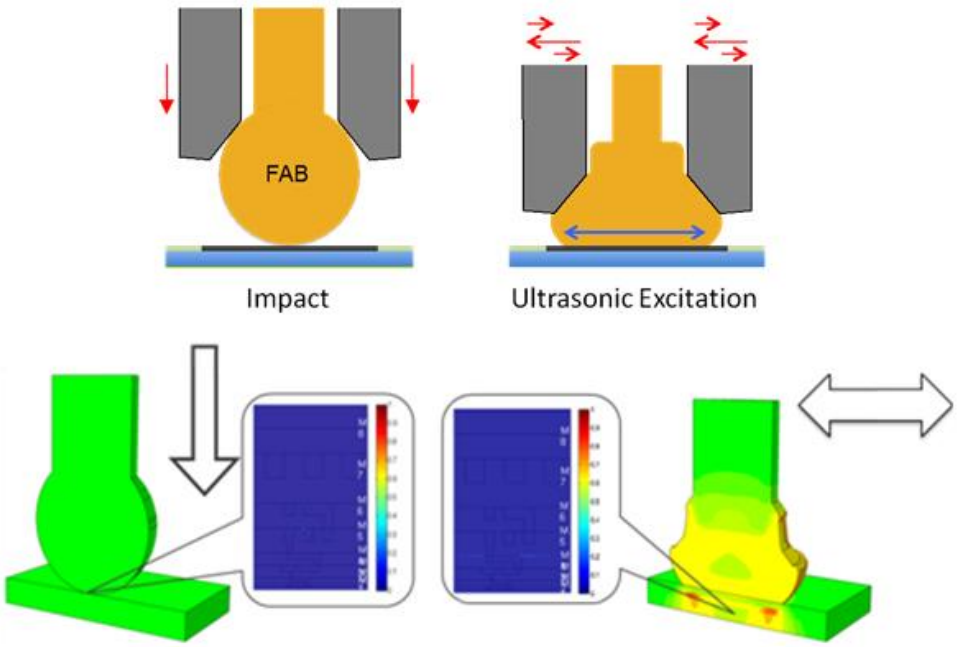

Figure 1-9. A multi-scale modeling approach as adopted by [15,16]. A 'global' wire bonding model is constructed using FEM approach, which provides boundary conditions for a 'local' isogeometric model which predicts crack nucleation.

The macroscale model results provide boundary conditions for a "microscale" model of the ILD stack built using a sophisticated "isogeometric" fracture modeling tool [18]. The microscale model is used to identify potential crack nucleation sites as well as the crack path within the ILD stack during wire bonding. The modeling also provides insight into the relative amounts of damage accumulated during the impact and the ultrasonic excitation stages.

CHAPTER 2. EXPERIMENTAL APPARATUS FOR MATERIAL CHARACTERIZATION

2.1 Overview

In this chapter, the need for a custom built microscale tester is discussed citing the inadequacy of the existing universal testers for characterizing the FAB. A microscale tester constructed to perform compression tests on the Cu FAB is described. The rationale for each component in the tester is then discussed, along with the LabVIEW program used to control the experimental environment. Uniaxial compression tests are then carried out on a known material at different temperatures, and the material properties obtained as result are validated against known values. The repeatability of results and accuracy of the microtester are also established.

2.2 Need for a Custom Tester

The components tested in the realm of electronic packaging are often few microns in size and often tend to exhibit a rate-dependent behavior. Also, to obtain sufficient data points to characterize a micron-sized object, the crosshead of the tester needs sufficient resolution. Further, a feedback loop is necessary in order to control proper motion of the crossheads at micron scale [19]. The material of the compressing punch must be significantly stiffer than the tested material. Furthermore, the surface finish must be sufficiently smooth, matching the scale of the specimen to ensure reliable test data. Ensuring parallelism between the faces of the punches is also a challenge, since extraneous loading must be eradicated in directions other than compression. Testing at such a scale also necessitates that the test be observed under high working depth microscope. Commercially available testers with the above capabilities are difficult to

find, and thus there is a need to construct an experimental apparatus with the mentioned abilities.

2.3 Hardware Components

The FAB is compressed between the faces of two punches as shown in Figure 2-2. Four materials of choice, steel, tungsten, tungsten carbide and titanium were compared based on the depth of indentation which a copper sphere of radius 25 μm would cause on a plane surface, assuming Hertz contact under a force of compression 0.1 N. Having the least depth of indentation, tungsten carbide was chosen as the punch material. In order to minimize frictional effects, the surface finishing operations were performed using diamond paste and colloidal silica to obtain a finish of 1 μm.

Table 2-1. Calculations on radius of contact of FAB and depth of indentation on the punch for different punch material. Tungsten carbide has the least depth of indentation.

Punch Material	Radius of contact(m)	Depth of indentation(m)
Steel	2.20685E-06	3.90E-07
Tungsten	2.05628E-06	3.38E-07
Titanium	2.41587E-06	4.67E-07
Tungsten carbide	2.01397E-06	3.24E-07

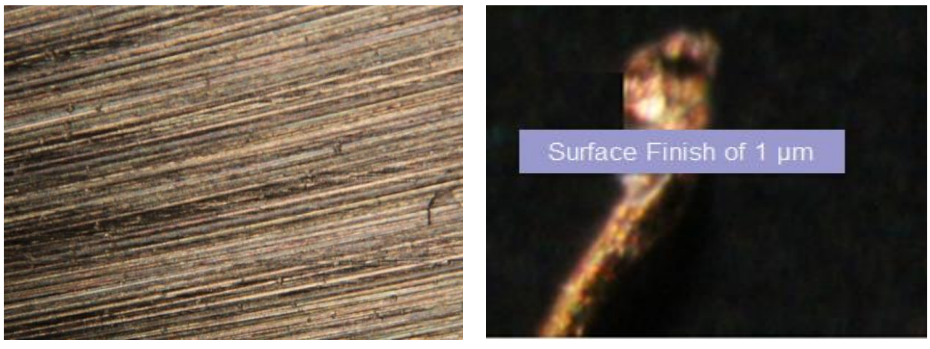

(a) (b)

Figure 2-1. (a) Surface of the tungsten carbide punch before surface finish operations (b) Surface of the tungsten carbide punch after surface finish operations with diamond paste and colloidal silica, shown with a Cu FAB on it.

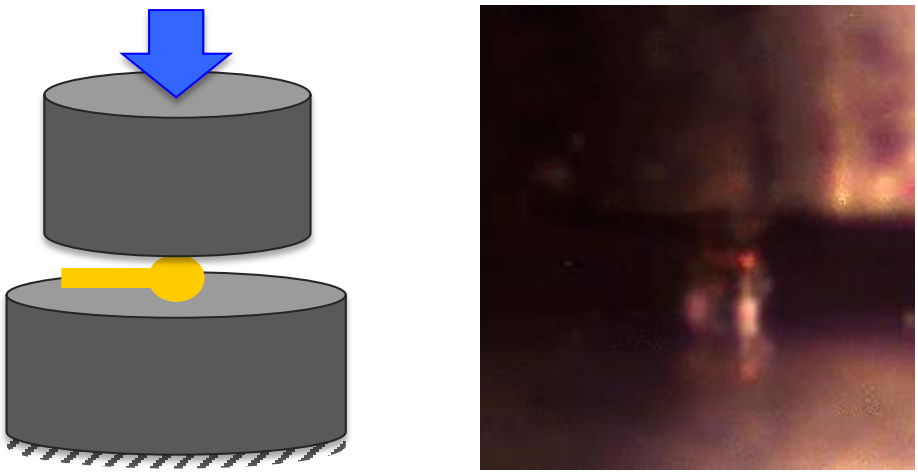

(a) (b)

Figure 2-2. (a) Schematic of a FAB positioned between the faces of the tungsten carbide punches (b) Compression test on the FAB between the punches viewed through a high working depth lens.

The lower punch is attached through interference fit to a cylindrical steel block of a larger diameter to prevent extraneous moments. This in turn is seated on a steel plate with fine surface finish, which is attached to a six-axis load cell. The load cell has a resolution of 50 mN along the axis of compression. The force resolution along the other axes is 20 mN, and the torque resolution along all the axes are 0.00015 Nm. The purpose of this load cell, hereafter referred to as load cell-1, is to measure extraneous loading which may arise due to misalignments.

Load cell-1 is seated on a tilt stage with resolution 2 arcseconds. This stage can withstand a load of 66 N, and has a range of ±4 ° tilt along all the axes. Its function is to maintain parallelism between the faces of the tungsten carbide punches. The tilt stage is mounted on linear stage of resolution 0.1 μm. Two such linear stages are mounted perpendicular to each other, effecting motions in the X and Y axes, aiding in the precise placement of the FAB under the top punch.

The upper tungsten carbide punch is attached to another load cell, hereafter referred to as load cell-2, of resolution 0.2 mN. The purpose of this load cell is to measure the compressive loads during the test. Load cell-2 is attached to a linear stage with resolution

0.03 μm, hereafter referred to as Z-stage. The resolution enables compressing the FAB of 25 μm diameter with sufficient displacement increments to characterize the material.

Attached to the Z-stage is a capacitance sensor with 0.008 μm resolution and a short range of 200 μm, and has two purposes. First, it provides a finer resolution in the displacement values, in between two discrete values of crosshead displacement readings. Second, it provides a closed-loop feedback to the PID controller in the LabVIEW program, which helps maintain the displacement rate of the crosshead a constant, irrespective of the load acting on it. The capacitance sensor outputs a voltage, which is converted into a displacement value based on a calibration factor. The calibration factor is obtained through the crosshead motion of the Z-stage when it is not under the influence of external loads. The compression tests are visualized with the aid of a 2-14X high depth lens (Figure 2-2(b)) and are recorded with a camera.

A thermoelectric Peltier device was later incorporated into the experimental set up between the support block and the base plate as shown in the Figure 2-4. The Peltier device was connected to the controlled power source and the purpose of this device was to control the temperature of the experimental environment. Temperatures up to 373 K were reached at the surface of the tungsten carbide punch using the peltier. Since the thermal mass of the FAB is negligible, the surface of the punch and the FAB were assumed to be at the same temperature. The Peltier uses thermoelectric heating effect, and only a single surface of the Peltier is heated by passing an electric current. The temperature at the surface of the bottom punch was monitored by a non-contact, off the shelf thermometer.

With the components described above, the issues of irregular crosshead motion, uniform loading in a single direction, appropriate surface finish for the punches, parallelism between the punches, possibility of tests at high-strain rates and visualization for the experiment were met.

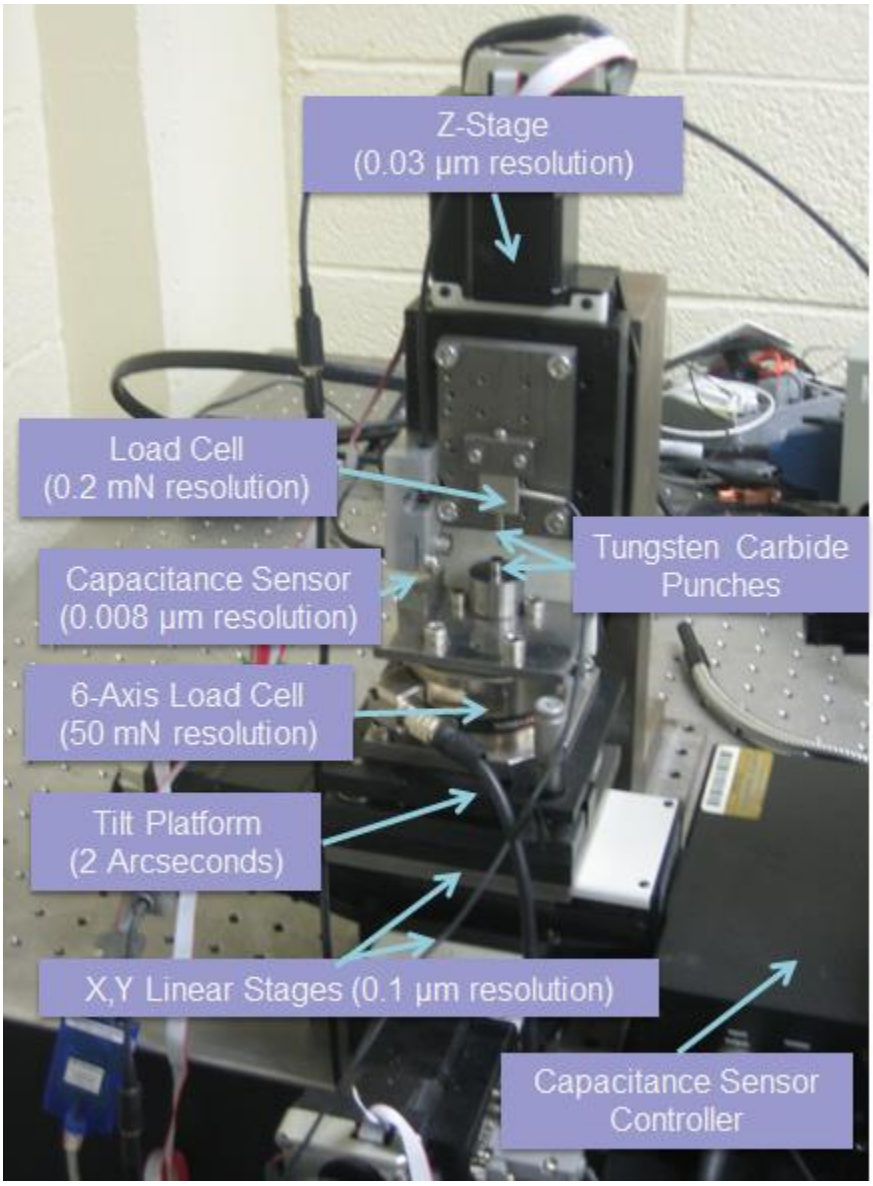

Figure 2-3. Experimental apparatus with three linear stages, one tilt stage, a capacitive stage with controller and two load cells. The FAB is compressed between the faces of the tungsten carbide punches.

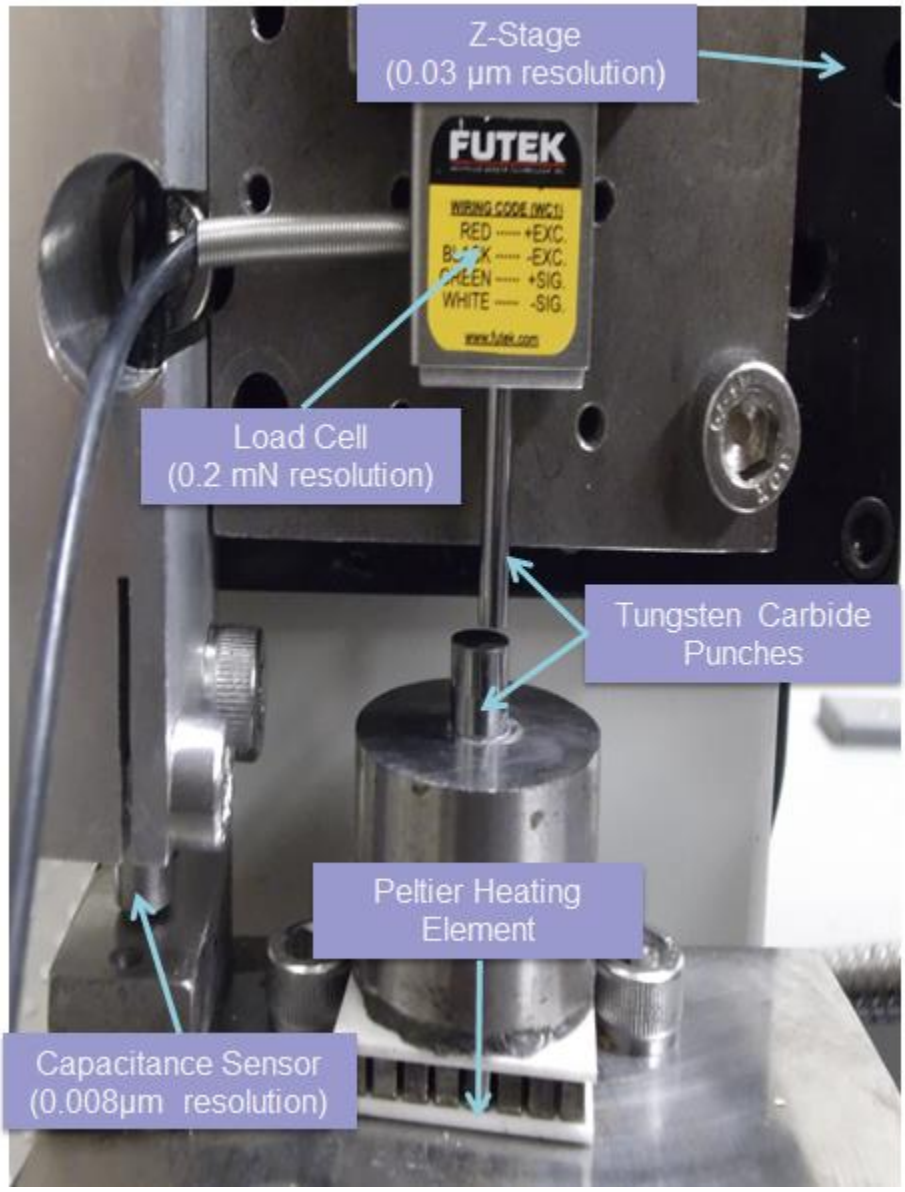

Figure 2-4. Apparatus with the Peltier heating element to perform compression tests at elevated temperatures.

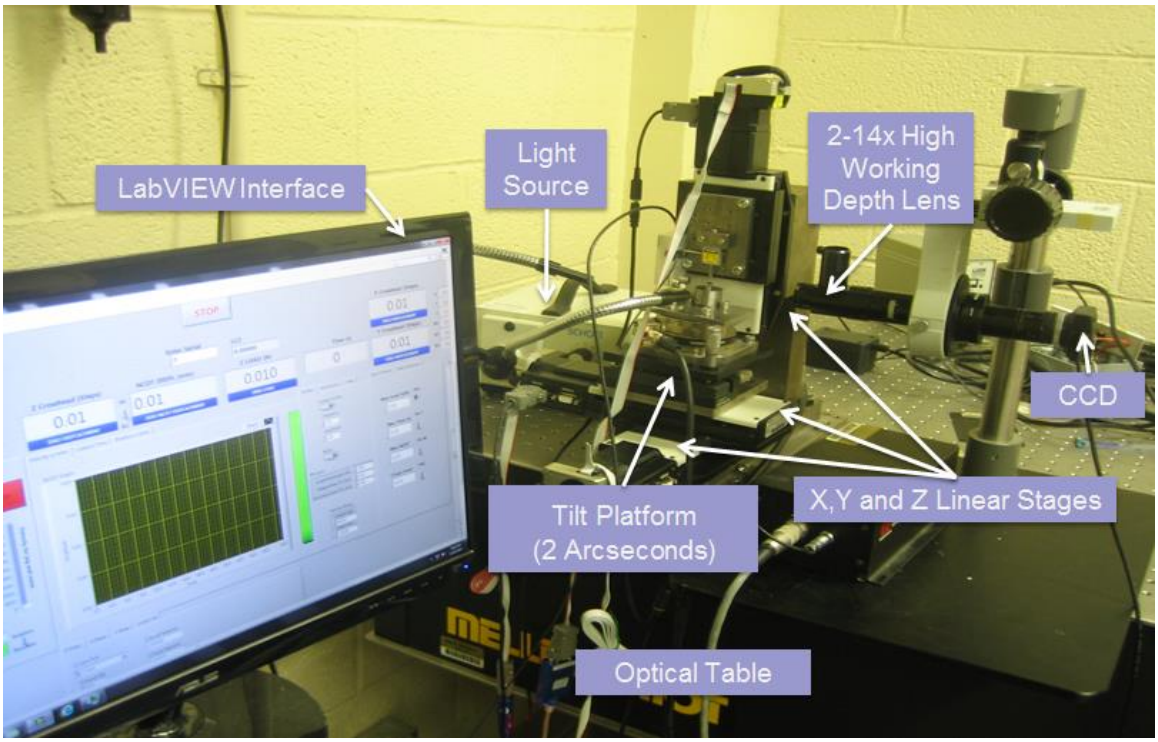

Figure 2-5. Experimental environment controlled by a LabVIEW program. Tests on FAB are viewed under a high-depth lens camera system.

2.4 Control Software

Since individual driver software for each component of the experimental apparatus was available under LabVIEW environment, LabVIEW was chosen as the software for experimental control. The control program as discussed in reference [19] was implemented. The front panel of the software has the following sub-panels (a) a manual adjustment to control the position of the linear stages (b) numerical display of the sensor readings (c) graphical display of the sensor readings (c) controls for monotonic test parameters (d) specimen protect (e) control for instrument interface.

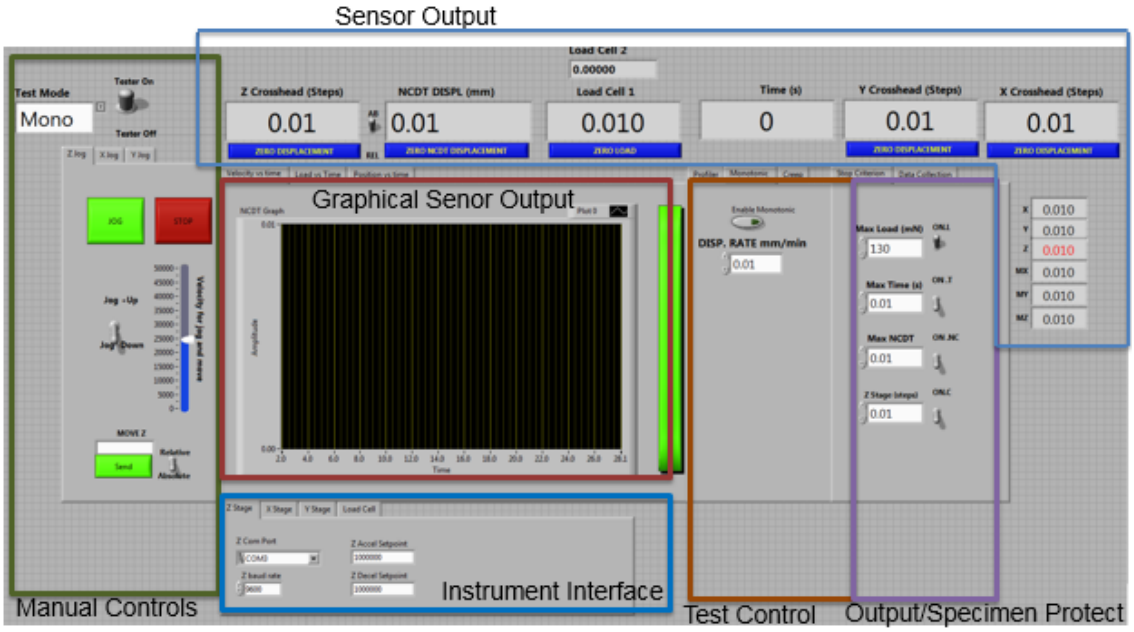

Figure 2-6. Software control interface for the experimental environment. Manual stages allow moving the stages to desired position before the tests. Test control specifies the monotonic test parameters. Specimen protect stops the loading when specified load thresholds are crossed. Numerical sensor output displays the sensor readings and graphical output plots them against each other.

The manual adjustment helps to 'jog' the X, Y and Z stages with a specified velocity, helping in the initial adjustments of the bottom punch, to position of FAB under the top punch. The test readings from load cell 1 and 2, crosshead readings from the three stages, readings from the capacitance sensor are displayed in the numerical display panel. These outputs are recorded in a text file at regular intervals during the test. The graphical display helps plotting the sensor readings versus each other. The uniform displacement rate and the PID values are provided as an input in the monotonic test controller. The PID controller takes input from the capacitive sensor, calculates the error between the applied and actual displacement rate and minimizes the error. The specimen protect enables to assign a maximum load, time or crosshead position, when reached, stops the crosshead motion.

2.5 Validation Tests

Compression tests were carried out on a cylindrical sample of Teflon PTFE, 1/8th of an inch in diameter and 2 mm in length, measuring its Young's modulus (E) at two different temperatures to validate the tester. For the purpose of validation, the values obtained from result are compared against the standard values supplied from the manufacturer's handbook. The tests were carried on two samples at 300 K and 373 K, at a constant rate of 0.1 mm/min.

In compression tests, the load train of the tester in itself is bound to have some compliance which influences the test results. In this case, the upper tungsten carbide punch will have a deformation of its own under the influence of the compression load. Thus, proper compliance correction measures must be applied in order to obtain the sample deformation.

$$\delta_{total} = \delta_{machine} + \delta_{sample} \tag{1}$$

The sample and the load train are treated as springs in series. The machine compliance is obtained by conducting compression tests without the sample, and is subtracted from the total compliance from the tests on the sample. The stress-strain curves obtained for Teflon PTFE after such corrective measures are shown in Figure 2-7.

The modulus values at room temperature differ from the manufacturer supplied value by 2% and 8% for the first and second sample respectively. The modulus values at 373 K vary from the standard value by 13% and 5% for the first and second sample.The values are found to be in agreement with the standard values. It has also been established that the tests are repeatable with considerable accuracy.

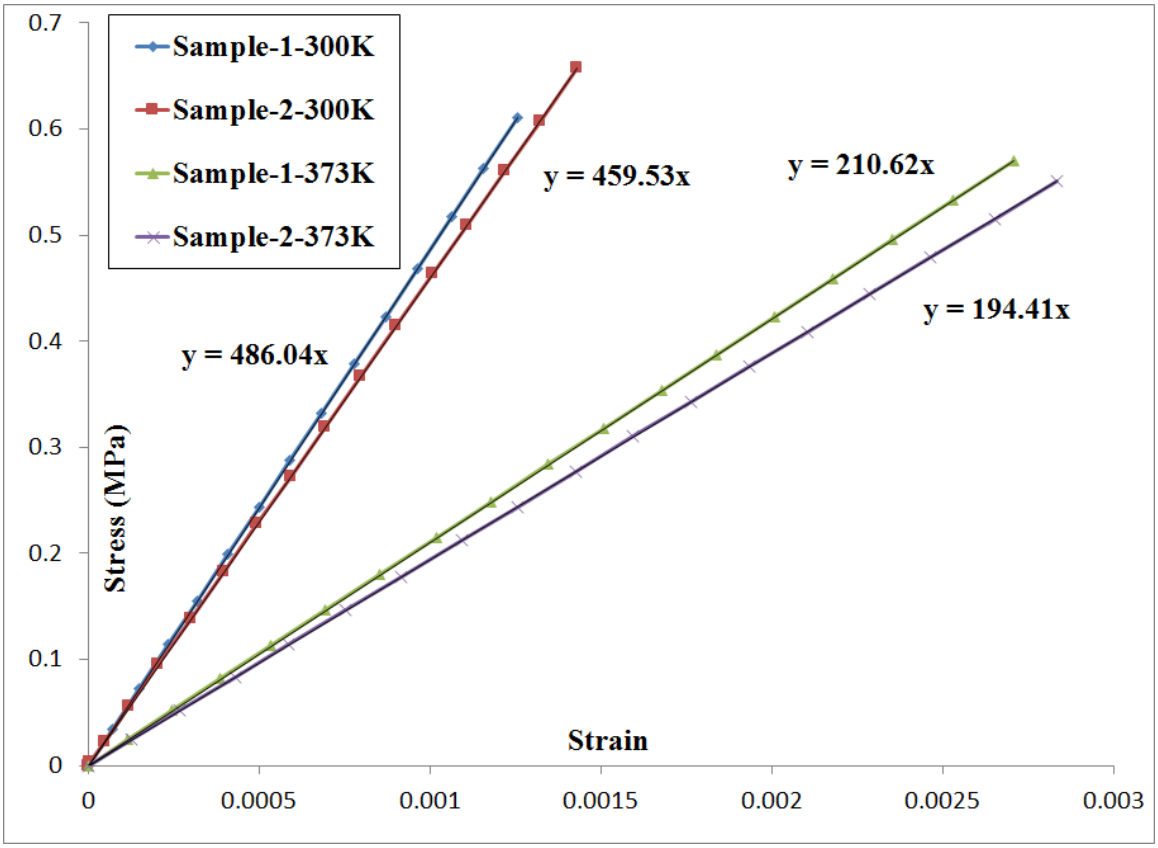

Figure 2-7. Stress vs Strain curves for Teflon PTFE tested at two different temperatures (300 K and 373 K) Two samples were tested at each temperature. Repeatability and the accuracy of tests are validated.

In summary, a microtester has been developed with a sub-micron resolution for displacement along all the axes, a capacitance stage with a sensor of sufficient resolution to measure such displacements, load cells with milliNewton resolution and tilt stage to ensure parallel faces of the punch. The test procedure could be viewed through a high depth lens system and recorded with the help of a camera. The the repeatability of results and the accuracy of the tester has been validated by measuring the modulus of Teflon PTFE.

CHAPTER 3. EXPERIMENTAL RESULTS

3.1 Overview

In this chapter, the experimental results of the compression tests on the FAB are presented. Three FAB samples were tested at room temperature at different strain rates and the force-displacement behavior was studied to observe the strain hardening effects. Then, the strain rate was maintained a constant and the effect of increasing temperature was studied.

3.2 Rate Dependent Behavior

Understanding strain rate and temperature dependent behavior of the FAB is particularly of interest, given the dynamic and high temperature nature of the wire bonding process. Rate dependent behavior in FCC metals such as copper has been documented by multiple researchers. Kocks and Follansbee [20], explored the axisymmetric behavior of Cu from strain rates 10^{-4} s^{-1} to 10^{4} s^{-1} and have proposed that the athermal dislocation effect or stage-II hardening effect are quite significant at high strain rates. Resistance to plastic deformation has also been noted to increase as the strain rate is increased [21]. Temperature is another factor playing a big role in dislocation dynamics of such material. Bordner and Merzer [22] have made viscoplastic constitutive equations for copper with a single internal variable, taking into account a range of strain-rates and temperatures. The wire bonding process could occur at temperatures over 250 °C, thus the effects of temperature on the mechanical strength of the FAB are an important aspect of study

The behavior of the FAB was studied in the low and intermediate strain-rate (0.001 s^{-1} - 4 s^{-1}), and at different temperatures (300 K -373K). Because of the spherical shape of the FAB and the large deformation nature of the experiment, it is difficult to obtain the

stress-strain data directly from the compression tests. Thus, the force-displacement (P-δ) behavior were obtained at different strain-rates, elastic and elasto-plastic contact laws were applied to verify if they explain the experimental behavior (Chapter 4). The P-δ plots at different rate, along with the polynomial curves of fit are shown in Figure 3-1.

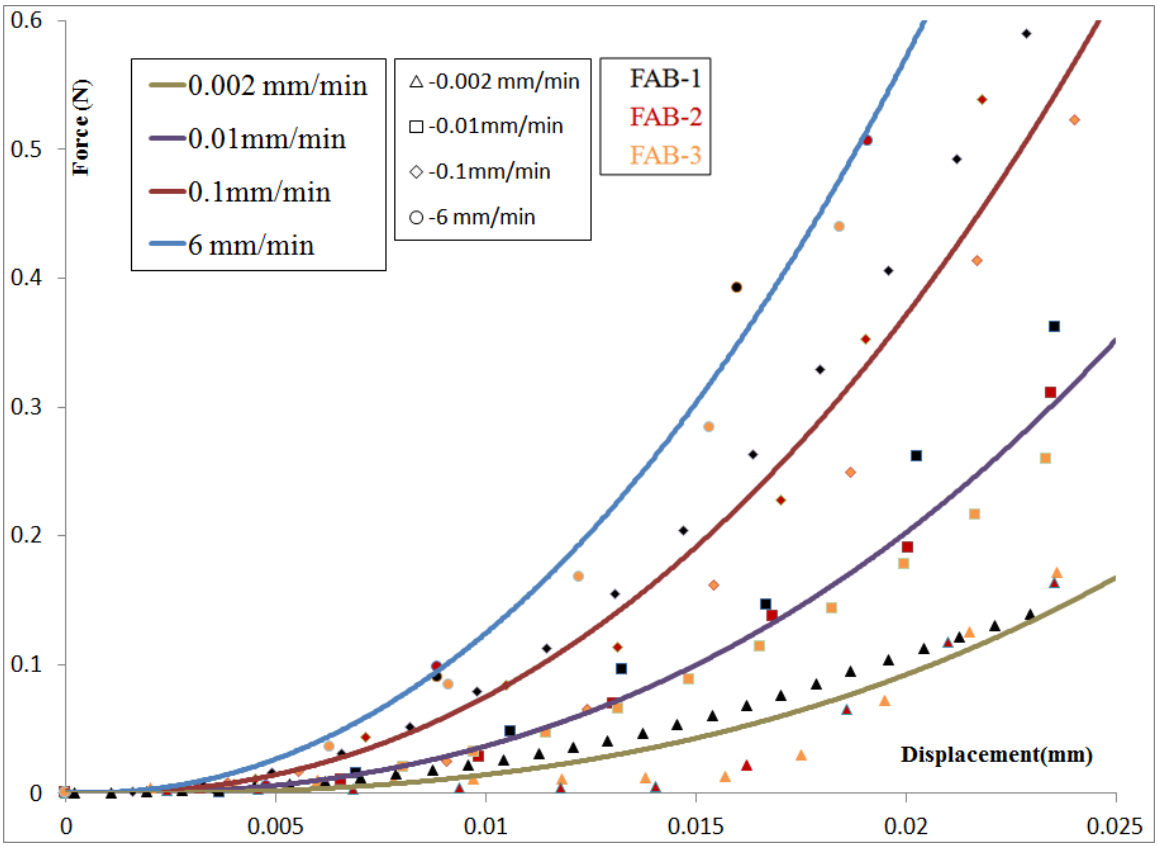

Figure 3-1. P-δ response of FAB under low and intermediate rates at room temperature. At higher rate, the force required to produce the same strain is higher.

Three FAB were tested at each rate to study the repeatability of results. It can be observed from the experiments that for a higher strain rate, larger forces are required to produce the same amount of strain. In other words, there is strain hardening effect, which is described in detail in Chapter 4.

3.3 Temperature Dependent Behavior

To study the dependence of the constitutive model parameters on temperature, the rate was maintained a constant (0.1 mm/min) and temperature was changed from 300 K to 373 K. The experimental *P-δ* plot along with the polynomial fit curves are shown in Figure 3-2. Two FAB were tested at each temperature to study the effect of temperature. It was noticed that with increasing temperature, the force required to produce the same amount of strain, at the same strain rate, was lower. Thus, temperature decreases the stiffness of the FAB.

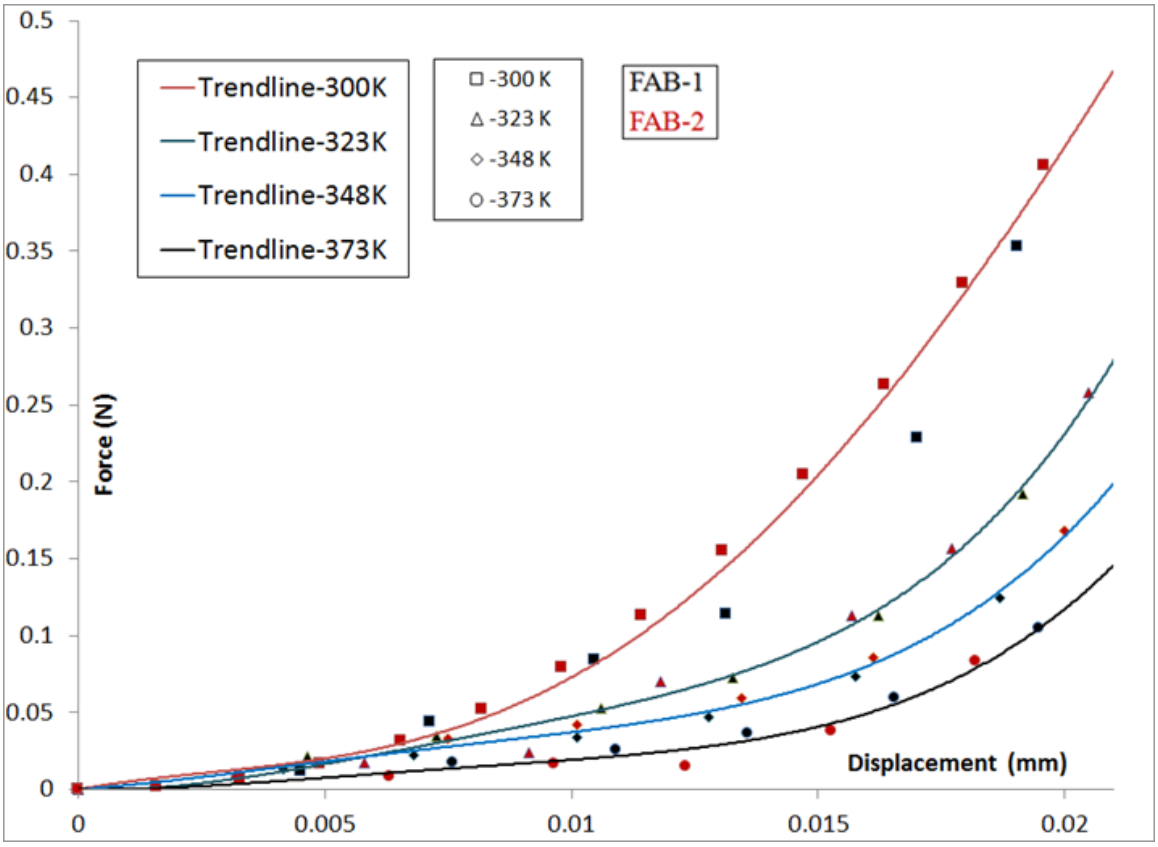

Figure 3-2. Compression tests on FAB at different temperature at a constant rate of 0.1mm/min. As the temperature increases, the force required to produce the same amount of strain in the FAB reduces.

In summary, the strain-dependent behavior of the Cu FAB was studied at low and intermediate strain rates. Multiple FAB were tested under different strain rates and a

strain hardening trend was observed. To study the effect of temperature, the strain rate was then maintained constant, and multiple FAB were tested from 300 K to 373 K. At higher temperature, the force required to produce the same amount of strain was lower. In the subsequent chapter, properties of copper are used to study elastic and elasto-plastic contact theories to see if they explain the experimental response.

CHAPTER 4. HERTZ CONTACT THEORIES AND EXTENSIONS

4.1 Overview

A short review of the elastic and elasto-plastic contact theories are presented in this chapter and are applied to the experimental plots to study if they fit the observed response. An analytical attempt is then made to understand the strain hardening effect by using a Ramberg-Osgood type stress-strain relationship and the strain hardening index is derived

4.2 Elastic Deformation-Hertz Model

While compressing the comparatively softer Cu FAB with a stiff and flat surfaced punch, the contact area is assumed circular under elastic limits. In most contact theories, the procedure to arrive at the *P*-δ relations is similar. The normal contact pressure, which of an assumed form, is integrated to obtain a relation between force and the contact radius. Then, through assumptions of elastic half space and mutual approach of distant points, a relation between displacement and contact radius is established. The contact radius is then eliminated between both equations, establishing a relation between force and displacement [23].

The pressure on a circular region is of the form [23]

$$p(r) = p_0\left(1 - r^2/a^2\right)^n, 0 \le r \le \text{a} \tag{2}$$

Where, n=1 for uniform pressure, n =-0.5 for uniform displacement and n=0.5 for Hertz pressure. Using Hertz pressure, the force of compression is obtained as

$$P = \int_0^a p(r) 2\pi r dr = \frac{2}{3} p_0 \pi a^2 \tag{3}$$

Where a is the contact radius and p_0 is the maximum pressure at the center of the contact area. Then, through assumptions of elastic half space, a relation between

normal displacement of the punch u_z and contact radius is established.

$$u_z = \frac{\pi p_0 (2a^2 - r^2)}{4aE^*} \tag{4}$$

Through theory of mutual approach of distant points, the normal displacement and the deformation, δ are related by

$$u_z = \delta - \left(\frac{1}{2\mathrm{R}}\right) r^2 \tag{5}$$

Equating the displacements

$$\frac{\pi p_0 (2a^2 - r^2)}{4aE^*} = \delta - \left(\frac{1}{2\mathrm{R}}\right) r^2 \tag{6}$$

Where R is the radius of the spherical FAB. Equating the coefficients and substituting for contact radius, we arrive at the relationship between force and deformation.

$$P = \frac{4}{3} E^* R^{1/2} \delta^{3/2}, \text{where } E^* = \frac{E}{1-\nu^2} \tag{7}$$

Predicted P-δ response by Hertz model, while using modulus and poison ratio for copper, is shown along with one set of experimentally observed values for different rates in Figure 4-4. The forces predicted by the elastic model are significantly higher than the experimentally observed values. It could be attributed to the fact that Hertz theory could be applied only to small strains, where the contact radius is comparatively much smaller than the radius of the sphere.

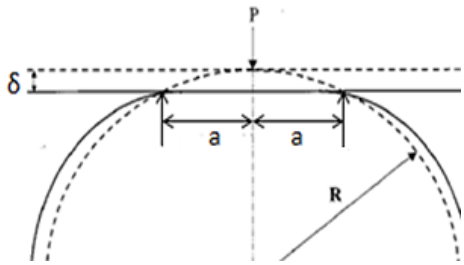

Figure 4-1. Hertz model for small deformation. A half-sphere undergoing a deformation of δ under the influence of the load P.

4.3 Large Elastic Deformation-Tatara Model

To investigate the effects of large deformation taking into account the lateral deformation of a rubber sphere, Tatara [24] proposed a set of five nonlinear equations relating the approach (γ), radii of contact (a'), the vertical position (z), the lateral extension of the contact area $U(z,a)$ and the radius of contact without lateral extension (a). It has been noted that for a sphere of radius 10 mm, Young's modulus of 1.2 MPa and poison's ratio of 0.48, Tatara's model was able to provide a close correlation towards experimental data till a load of 5000 N, whereas Hertz theory was only applicable till 50 N [25].

The radius of contact, taking into account the lateral expansion of sphere is given by

$$a' = a + U(\mathrm{z}, \mathrm{a}) \tag{8}$$

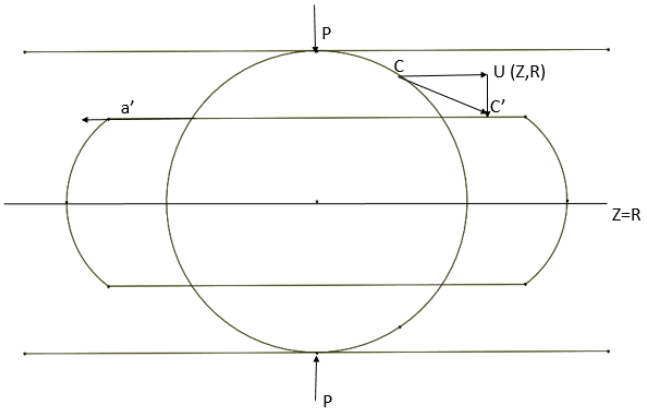

Figure 4-2. Sphere compressed by rigid punch. Adopted from Tatara model [24]

The relation between vertical position and contact radius without taking into effect the lateral extension

$$z = R - \sqrt{R^2 - a^2} \tag{9}$$

The approach is given by

$$\gamma = A\frac{3(1-\upsilon^2)}{4E}[1+\frac{Ba'^2}{8R^2[1+U(z,a)/a]^2}]\frac{P}{a'} - \frac{f(a')A}{\pi E}[1+\frac{Ba'^2}{5R^2[1+U(z,a)/a]^2}]P \quad (10)$$

Where $A=\frac{(1-\xi)^2}{1-\xi+\xi^2/3}$, $B=\frac{(1-\xi/3)}{1-\xi+\xi^2/3}$, $f(a)=\frac{2(1+\upsilon)R^2}{(a^2+4R^2)^{3/2}}+\frac{1-\upsilon^2}{(a^2+4R^2)^{1/2}}$ and $\xi=\gamma/R$

The lateral extension of the contact area is related to the vertical position through

$$U(z,a)=\frac{A(1+\upsilon)P}{2\pi E}[1+\frac{Ba'^2}{5R^2[1+U/a]^2}]$$

$$\text{x}[\frac{\sqrt{z}+\sqrt{2R-z}}{2R\sqrt{2R}}-\frac{1-2\upsilon}{\sqrt{2Rz(2R-z)}}(2\sqrt{2R}-\sqrt{Z}-\sqrt{2R-z})] \quad (11)$$

And finally, the relation between load and vertical position is given by

$$z=A[\frac{3(1-\upsilon^2)}{8Ea}(1-\frac{Ba^2}{2R^2})+\frac{Bf(a)a^2}{2\pi ER^2}]P \quad (12)$$

The preceding five non-linear equations [24] are solved using fsolve in MATLAB for each load. Though Tatara's theory predicts a realistic contact radius at higher loads, the forces predicted by the model coincide with the ones predicted by Hertz model. The *P-δ* response predicted by this model is shown along with the experimentally observed values in Figure 4-4.

4.4 Elasto-Plastic Deformation

As the contact force increases, the stresses in the Cu FAB eventually reach the point of yielding. Thornton [26] suggested that the contact pressure distribution follows Hertz law until the critical limit, beyond which the onset of plastic yielding occurs and the pressure distribution follows a truncated pattern. Johnson [23] arrived at the critical load and displacement at which this occurs using Von Mises criteria. He calculated the critical pressure at which this happens as 1.6Y, where Y is the yield strength of the material. The corresponding critical displacement and force given by that value of pressure are

$$\delta_y = \frac{1}{4}\frac{\mathrm{R}}{E^{*2}}(\pi Y)^2 \tag{13}$$

$$P_y = \frac{1}{6}\left(\frac{\mathrm{R}}{E^*}\right)^2(\pi Y)^3 \tag{14}$$

The values of critical force and displacement were calculated to be $7.6\text{x}10^{-9}$ mm and $1.4\text{x}10^{-8}$ N respectively[16]. Thus, all the measurements made could be assumed to be in the plastic region. Thornton [27] subtracted the yield stress from the hertz pressure and obtained post-yield *P-δ* relation using the following procedure.

$$P = P_e - \int_0^{a_p} 2\pi(p(r) - \sigma_y)r\,dr \tag{15}$$

Where P_e is the elastic Hertz force from Equation(7) Substituting for pressure from Equation (2) we have

$$P = P_e + \pi\sigma_y {a_p}^2 - 2\pi p_0 \int_0^{a_p} r\left(1 - \left(\frac{r}{a}\right)^2\right)^{1/2} dr \tag{16}$$

The integral term on the right hand side could be calculated as

$$\int_0^{a_p} r\left(1 - \left(\frac{r}{a}\right)^2\right)^{1/2} dr = -\frac{1}{3}a^2\left[\left(1 - \left(\frac{r}{a}\right)^2\right)^{3/2}\right]_0^{a_p} \tag{17}$$

Substituting (17) in (16) we get

$$P = P_e + \pi\sigma_y {a_p}^2 - \frac{2}{3}p_0\pi\mathrm{a}^2 + \frac{2}{3}p_0\pi\mathrm{a}^2\left(1 - \left(\frac{a_p}{a}\right)^2\right)^{3/2} \tag{18}$$

Substituting (3) in (18)

$$P = \pi\sigma_y {a_p}^2 + P_e\left(1 - \left(\frac{a_p}{a}\right)^2\right)^{3/2} \tag{19}$$

Where a_y is the plastic contact radius, P_y is the plastic contact force and a_p is the contact radius over which uniform pressure is assumed.

Following the logic in Equation (3)

$$P_y = \frac{2}{3}\sigma_y \pi {a_y}^2 \tag{20}$$

Following the logic in Equation (2) and Figure 4-3 we have

$$\sigma_y = \frac{3P_e}{2\pi a^2}\left[1-\frac{a_p^{\,2}}{a^2}\right]^{1/2} \tag{21}$$

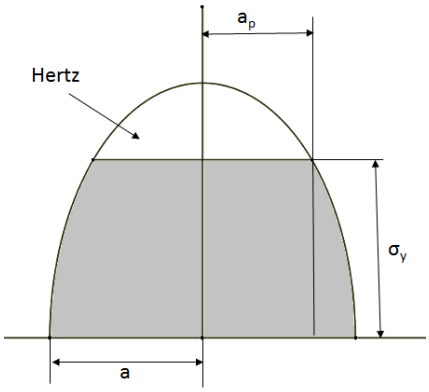

Figure 4-3. Normal traction distribution in Thornton Model adopted from [27].

Substituting (21) in (20) and substituting the value of contact radius *a* we get

$$\left[1-\frac{a_p^{\,2}}{a^2}\right]^{1/2} = \left[\frac{a_y}{a}\right]^2 \tag{22}$$

Substituting (22) in(19), and substituting for the contact radius, the post-yield *P*-δ is given by

$$P = P_y + \pi YR(\delta - \delta_y) \tag{23}$$

The response predicted by Thornton model is shown along with the other contact models in Figure 4-4. Though the magnitude of the predicted forces was comparable in value to the observed experimental values, Thornton model predicts a linear *P*-δ response, which does not match the observed response. Thus, development of new material model for the FAB is justified. In the next section, an analytical approach is adopted to deduce the strain-hardening index.

4.5 Constitutive Modeling

In the analytical approach, a constitutive model that allows one to express stress as a function of strain is first chosen. The relationship is substituted in lieu of the material parameter in one of the contact laws, so that the law is modified to 'fit' the observed response in the experiments.

A Ramberg-Osgood Law [28] type relationship was first attempted to express the stress as a parameter of strain.

$$\varepsilon = \frac{\sigma}{E} + \beta \frac{\sigma_y}{E} \left(\frac{\sigma}{\sigma_y} \right)^a \tag{24}$$

In the above equation, σ and ε are the stress and strain along axis of compression, σ_y is the yield strength, and E is the Young's modulus. In the case of large deformation, that too for material like copper [28], the elastic part of the equation can be removed, thus, a direct stress strain relation of the following form is achieved.

$$\sigma = C\varepsilon^m \tag{25}$$

Where $C = \frac{1}{\beta} \frac{E}{\sigma_y}$ and $a=1/m$. The secant modulus E_s could be obtained by

$$\left(\frac{\sigma}{\varepsilon} \right) = C\varepsilon^{m-1} = E_s \tag{26}$$

By replacing Young's modulus by Secant modulus and substituting the above relation in (23)

$$P = \frac{1}{6} \left(\frac{R}{C\varepsilon^{m-1}} \right)^2 (\pi Y)^3 (1-\nu^2)^2 + \pi YR\delta - \frac{1}{4} \left(\frac{R}{C\varepsilon^{m-1}} \right)^2 (\pi Y)^3 (1-\nu^2)^2 \tag{27}$$

$$= \pi YR\delta - \frac{1}{12} \left(\frac{R}{C\varepsilon^{m-1}} \right)^2 (\pi Y)^3 (1-\nu^2)^2 \tag{28}$$

The above form of force is equated with the experimental curves to obtain the value of the strain-hardening index. A non-linear regression analysis is done on the experimental plots to obtain values of K and n to fit the curve of the following form.

$$P = K\delta^n \tag{29}$$

The values of n are shown in the Figure 4-4. Equating (29) and (28)

$$K\delta^n = \pi YR\delta - \frac{1}{12}\left(\frac{R}{C\varepsilon^{m-1}}\right)^2 (\pi Y)^3 (1-\nu^2)^2 \tag{30}$$

Substituting strain $\varepsilon = \frac{\delta}{D}$, where D is the diameter of the FAB and equating the powers of δ on both sides of the equation, we arrive at the following strain hardening index *m* for different rates as shown in Table 4-1 .

Table 4-1. Strain hardening index *m* for different rates.

V (mm/min)	0.002	0.01	0.1	6
n	2.67	2.47	2.34	2.2
m	0.33	0.23	0.17	0.10

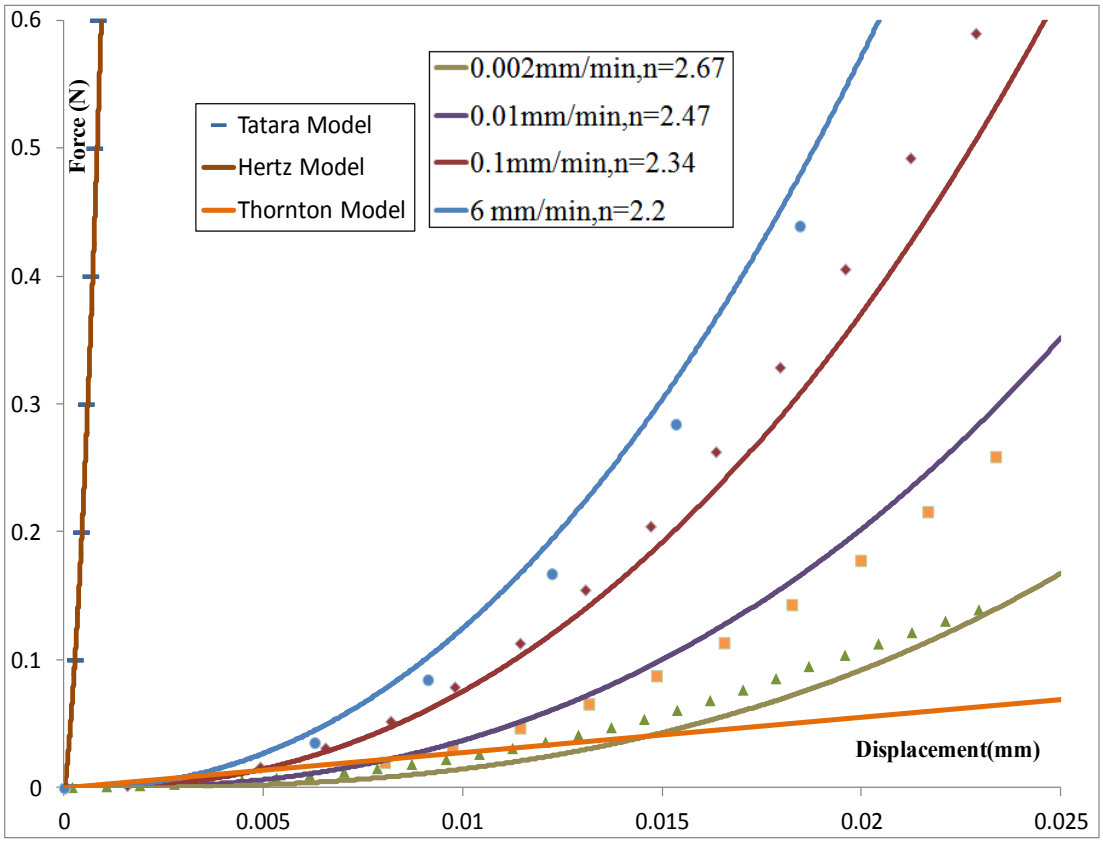

Figure 4-4. Hertz, Tatara and Thornton models fail to predict the behavior of FAB. A fit of the form $P = K\delta^n$ used to obtain the value of *n*.

As a characteristic of viscoplastic material, the stresses of the FAB increase with the increase in strain rate, for the same amount of strain. The compressive tests reveal a strain hardening effect. Strain hardening is not so pronounced as the experimental strain rates are increased, which could be noted by the increments in the value of *m* in Table 4-1.

The concept of yield surface plays a pivotal role in plasticity. For a material such as copper, the concept of yield limit is no longer strictly applicable even in the absence of rate effects and the stress-strain curves contain no discernible elastic limits [28]. Thus, 'unified' models in which yield is a consequence of the constitutive law itself are chosen to explain the behavior of the FAB in subsequent chapters.

CHAPTER 5. UNIFIED VISCOPLASTIC MODEL

5.1 Overview

The theories of viscoplasticity describe the rate-dependent behavior of a material. Viscoplastic materials differ from rate-independent plasticity in one aspect, for same strain, the stress is higher for a higher strain rate. Viscoplastic behavior can be attributed to metals that show no discernible elastic limits or yield point, and show highly nonlinear, rate-dependent behavior especially at high temperatures. A brief review of viscoplastic materials are provided in this chapter and the appropriate model is chosen to characterize FAB behavior.

5.2 A Review of Viscoplastic Models

A sizable literature exists on viscoplastic laws, such as the models by Hart, Busso, Krempl, Anand, McDowell and Ishikawa. Most of these viscoplastic models arise from Kock's discussion about thermodynamics of slip [29]. The choice of model entirely depends upon the ability of the model to explain the observed set of material behavior. In both rate-independent plasticity and in viscoplasticity, the concept of yield surface plays a pivotal role [30]. Many models, like those of McDowell [31], [32] and Ishikawa [33] use the yield surface approach, and thus might not be suitable to characterize the FAB. For materials such as copper, the concept of yield limit is no longer strictly applicable even in the absence of rate effects and the stress-strain curves contain no discernable elastic limits [30]. Thus, a 'unified' viscoplastic model was chosen to characterize the behavior of copper FAB.

In unified theories, yielding is not a separate criterion, but a consequence of constitutive law. Such theories are used to predict the monotonic, cyclic and creep behavior. Viscoplastic theories by Hart, Busso, Krempl, and Anand model fit this criterion. Between these models, the choice depends on the following factors.

- The chosen model must be able to explain the material behavior at a wide variety of strain rates and temperatures.
- Must have tractable number of state variables and material parameters.
- The model must be able to predict the experimental behavior that was not used to calibrate the parameters.

Hart [34] described relations between applied deviatoric stress, non-elastic strain rate and two state variables. One of the state variables is a scalar, σ^* and describes the isotropic strain hardening. The second state variable is a tensor a representing the history and magnitude of the stress. The equations of Hart have been presented below.

The constraint equations in the model are

$$\dot{\varepsilon} = \dot{a} + \dot{\alpha} \tag{31}$$

$$o = o_a + o_f \tag{32}$$

Where o_a and o_f are the stress operatives in each branch. The relations between the tensors are given by

$$a = (a/\sigma_a)o_a \tag{33}$$

$$\dot{\varepsilon} = (\dot{\varepsilon}/\sigma_f)o_f \tag{34}$$

$$\dot{\alpha} = (\alpha/\sigma_a)o_a \tag{35}$$

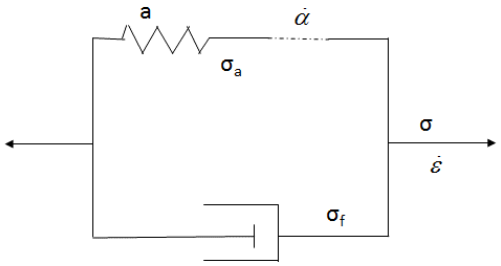

Figure 5-1. Schematic representation of Hart's model adopted from [34].

And scalar relations are given by

$$\dot{\varepsilon} = \dot{a}^*(T)(\sigma_f/\mu)^M \tag{36}$$

$$\ln(\sigma^*/\sigma^a) = (\dot{\varepsilon}/\dot{\alpha})^\lambda \tag{37}$$

$$\dot{\varepsilon}^* = (\sigma^*/G)^m f(e^{(-Q/RT)}) \tag{38}$$

$$\sigma_a = \mu a \tag{39}$$

$$d\ln\sigma^*/dt = \Gamma(\sigma^*,\sigma_a)\dot{\alpha} - \varsigma(\sigma^*,T) \tag{40}$$

Thus, the parameters which have to be evaluated by experiments are μ, M, m, λ, f, Q and G. There are three functions to be evaluated by experiments, Γ, a^* and ς .

The difficulties with Hart's model are the following. The material parameters are to be determined by uniaxial loading and load relaxation tests are to be carried out as well. The model also requires tracking the history of these parameters. Given the geometry and size of the FAB, carrying out the tests to determine the parameters become difficult.

In place of the Hart's hardening parameter, Busso's constitutive model [34,35] has a back stress or internal stress B to capture the macroscopic kinematic hardening due to dislocation barriers, defined by the following relation

$$\dot{B} = h\dot{\varepsilon}^p - rB\left|\dot{\varepsilon}^p\right| \tag{41}$$

Where h is the hardening modulus and r is the recovery coefficient .The expression for the inelastic strain rate is given by the following relation

$$\dot{\varepsilon}^p = \dot{\varepsilon}_0 \exp\left\{-\frac{F_0}{R\theta}\left[1-\left(\frac{|\sigma - B|}{\sigma_0 G/G_0}\right)^p\right]^q\right\} sign(\sigma - B) \tag{42}$$

In this model, there are ten material parameters, five that are intrinsic properties of the material, including σ_0 - the yield stress at 0 K, F_0 - activation energy at 0 K, G-shear modulus, α-coefficient of thermal expansion and k -bulk modulus. The remaining five parameters are $\dot{\varepsilon}_0$-strain rate, p and q -exponents, h and r. This model does not serve the purpose since the many of these properties of the FAB are again to be determined by monotonic or cyclic tests. Krempl's theory [36–38] of viscoplasticity is the most complex of the theories discussed. The Viscoplasticity Based on Overflow (VBO) model, has three state variables and seventeen material parameters, which in turn vary with time, to be determined through similar tests as with the models discussed earlier. Unlike the previous models, it does not take into

considerations the strains due to dislocations, however, it introduces a viscoplastic flow potential to arrive at the governing equations.

5.3 Anand Model

To explain the rate-dependent deformation of metals at high temperature Anand [40] proposed a viscoplastic model with a single internal variable and with nine material parameters . The model has been successfully applied to explain the behavior of solders [41] and hot working of many metals [42]. To determine these parameters, usually one would require steady state creep tests and tensile tests at different temperatures and strain rates, but the model's availability in commercial finite element packages allows us to do an inverse modeling to fit the parameters.

Anand model has one scalar internal variable '*s*', which captures the 'averaged isotropic resistance' [40] to plastic flow due to strengthening mechanisms such as dislocation density and grain size effects [41].

There are two governing equations in the model. The first is the plastic flow equation

$$\dot{\varepsilon}^p = A\left[\exp\left(\frac{-Q}{R\theta}\right)\right]\left(\sinh\xi\frac{\sigma}{s}\right)^{\frac{1}{m}} \tag{43}$$

And the second is the evolution equation for the internal variable *s*

$$\dot{s} = h_0\left(sign\left(1-\frac{s}{s^*}\right).\left|1-\frac{s}{s^*}\right|^a\right)\dot{\varepsilon}^p \tag{44}$$

$$s^* = \hat{s}\left[\frac{\dot{\varepsilon}^p}{A}\exp\left(\frac{Q}{R\theta}\right)\right]^n \tag{45}$$

Thus, there are nine material parameters to evaluate. $A, Q/R, a, m, n, h_0, \hat{s}, \xi$ and s_0. The stress along the axis of compression is denoted by σ . A is the pre-exponential factor. It is similar to the first order frequency-factor of Arrhenius type rate equation, representing a rate constant, having units of a strain rate. Q is the activation energy and R is the universal gas constant, the ratio Q/R is a single parameter. Parameter h_0 is the hardening or the softening parameter. Parameter $\hat{s}$ is a coefficient, s^* is the

deformation resistance saturation value, s_0 is its initial value, all with the units of stress. The rate sensitivity h_0, s^* and σ are represented by *a, n* and *m* respectively. ξ is a dimensionless stress multiplier. When the value of internal variable *s* reaches the saturation value s^*, the evolution of the internal variable equation, Equation(44), is of no significance. Equation (43) then reduces to a Hyperbolic-Sine law, which is of the following form

$$\dot{\varepsilon}^p = A\left[\exp\left(\frac{-Q}{R\theta}\right)\right]\left(\sinh \xi\sigma\right)^{\frac{1}{m}} \tag{46}$$

The procedure to fit Anand constants follow. First, the saturation value of the stress is to be deduced from the constant strain rate and temperature tests. Then, Parameters *Q/R, A, m,* $\hat{s}/\xi$ and *n* through a nonlinear fitting method of the following of steady state creep results to the following equation [41].

$$\sigma^* = cs^* = \frac{\hat{s}}{\xi}\left[\frac{\dot{\varepsilon}^p}{A}\exp\left(\frac{-Q}{R\theta}\right)\right]^n \sinh^{-1}\left[\exp\left(\frac{-Q}{R\theta}\right)\right]^m \tag{47}$$

The individual parameters $\hat{s}$ and ξ are obtained by fitting ξ to the constraint that the value of constant *c* has to be less than one in Equation(49).

The values of *a,* h_0 and s_0 are fit from the monotonic tests fitting the following relation.

$$\sigma = \sigma^* - \left[(\sigma^* - cs_0)^{(1-a)} + (a-1)\left\{\left(ch_0\right)\left(\sigma^*\right)^{-a}\right\}\varepsilon_p\right]^{\frac{1}{1-a}} \tag{48}$$

Where

$$c = \frac{1}{\xi}\sinh^{-1}\left[\left(\frac{\dot{\varepsilon}_p}{A}e^{\frac{Q}{RT}}\right)^m\right] \tag{49}$$

5.4 Inverse Finite Element Model

As established before, neither monotonic tensile tests nor steady state creep tests can be performed to obtain the parameters directly. However, Anand model is available in both major commercially available software, ABAQUS and ANSYS. Thus, an axisymmetric finite element model is created to simulate the compression

tests, and the material parameters are iterated till *P-δ* curves obtained from FE model matches with the experimental results.

In ANSYS, a quarter circle axisymmetric around Y-axis was constructed and meshed with PLANE182 elements. The tungsten carbide punch was modeled using rigid TARGE169 elements, and a single node-to-node connection was established as initial contact between the two parts. The circumference of this circle was populated with CONTA172 elements to simulate the evolving contact radius as the compression tests proceed. A constraint equation was prescribed in the Y-direction for all the nodes at Y=0, coupling them a master node N. This would satisfy two purposes. First, the displacement applied on node N is applied uniformly to all the nodes at Y=0. Second, it would avoid the procedure to sum the individual forces on each node at Y=0 to obtain the total force of the compression. The force at node N will be the required resultant force. Anand's model is directly available as material option and could be invoked by the command TB,RATE,,,9,ANAND. The nine constants are then defined as per the documentation [43]. A uniform body temperature of 300 K is prescribed throughout the area. Displacement conditions were applied on node N and different time steps were specified in individual simulations to simulate tests at different strain rates.

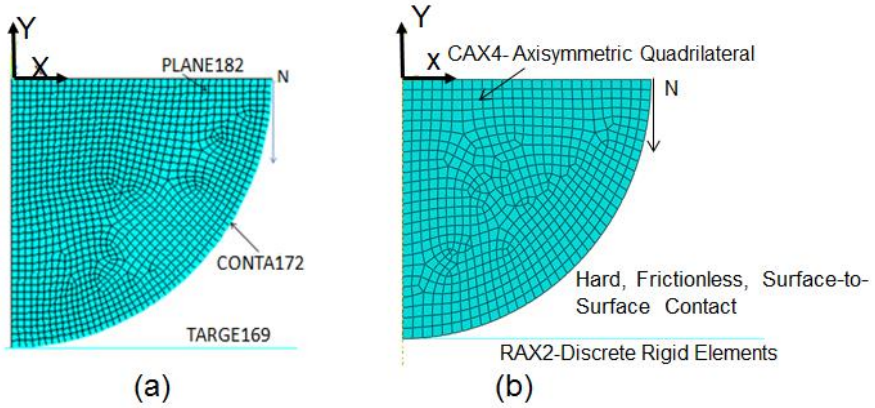

Figure 5-2. (a) Axisymmetric finite element model in ANSYS meshed with PLANE182 elements. TARGE169 and CONTA172 elements capture the behavior of rigid punch and evolving contact radius (b) Axisymmetric finite element model in ABAQUS meshed with CAX4 elements, RAX2 rigid elements serve as the punch and surface to surface contact discretization is used.

In ABAQUS, a similar geometry was constructed axisymmetric about Y-axis and meshed with CAX4, axisymmetric, linear 4 node quadrilateral elements. RAX2, discrete axisymmetric, rigid link with a reference point in the middle was used to simulate the tungsten carbide punch. In ABAQUS, Anand model is directly available in version 6.14, and could be invoked by prescribing the user defined creep law, and changing the keyword USER to ANAND and including the constants in the two lines that follow as

*CREEP, LAW=ANAND

$s_0, Q/R, A, \xi, m, h_0, \hat{s}, n$

a

A mention has to be made that the above-described form of Anand law is only a reduced form of the 'modified' version of Anand law, which will be described in detail in later sections, whilst deriving the temperature dependent material parameters.

In earlier versions of ABAQUS, Anand law could be invoked by an in-built user subroutine, by editing the keywords in the following manner. The material is renamed as

*MATERIAL, NAME=ABQ_CREEP_MOD_ANAND

And the *CREEP keyword is editing as follows

*CREEP, LAW=USER

$s_0, Q/R, A, \xi, m, h_0, \hat{s}, n$

$a, T0$

Where $T0$ (0 K) is the reference temperature. This parameter is not required in version 6.14, since it is prescribed in the model definition. In earlier versions, the number of dependent variables has to be specified, which is one in case of Anand model.

*DEPVAR

1,

The temperature (300 K) is prescribed as a predefined field and surface-to-surface contact are defined in the initial step. The rigid surface serves as the master surface and the slave surface is the circumference of the circle. Displacement conditions were prescribed on the line at Y=0 and the forces of compression could be obtained by

recording the resultant force history at the reference point of the rigid line. Different step times are prescribed during load step to simulate rate effects.

During the compression test, the applied rate corresponds to the velocity of motion of the point on the spherical FAB in contact with the rigid punch. However, the displacement boundaries in the FE model are applied to an outermost node of the midline of the half-sphere in the FE model, thus the applied rate in the FE model is half the actual rate. To obtain actual displacement of the FAB, the displacement of node N was multiplied by two. This was later verified by constructing full-circle axisymmetric and 3D models, and the results were in agreement. The reduced model significantly reduces the time while performing material parameter optimization, which takes several hundred runs as described in later sections.

The results obtained through ABAQUS and ANSYS were nearly identical, though the physical problem was modeled by different finite element approximations, contact definitions and enforcements, and boundary constraints. More than a verification, the model was reconstructed in ABAQUS because of the seamless integration of its FE module to the optimization tool, Isight. ANSYS workbench optimization does not have array capabilities at present time. Such a capability is required to extract an array of P-δ results from the FE simulation and to compare it with the array of experimental P-δ using definite objective to minimize the differences between them.

5.5 Material Parameter Optimization

Given that there are nine parameters that have to be iterated in order to arrive at the ‘optimal’ parameter set to describe the observed behavior, there is wide choice of parameter values that may non-uniquely lead to the observed behavior. Referring to Equations(43), (44) and (45) one can observe that these parameters influence the results in a nonlinear fashion, thus optimization to fit one parameter at a time is not feasible. Moreover, the material parameters have to describe experimental responses at all the strain rates and temperatures. Thus, an automated optimization procedure has to be constructed to determine the material constants.

To formulate a successful optimization problem, the range of values for the individual parameters (i.e., the design space) has to be first identified for the material

parameters with the following two constraints. First, these parameters have to be physically feasible and must be permitted by the constitutive equations, for instance $a>1$. Second, the bounds must be able to explain the range of P-δ behavior observed at both low and intermediate strain rates. A robust initial point must also be specified for the optimization algorithm to achieve a faster convergence.

To decide on the bounds of the material parameter, a set of parameters were obtained from literature. These Anand model material data have been derived for copper by Anand [44], and a sizable literature exists characterizing solder material using this law. Typical Sn-Ag solder alloy material parameters produce P-δ in the observed range of the FAB [40,44]. These parameters were taken as an initial guess, and were varied individually to arrive at the upper and lower bounds for the material parameters, constructing a design space of desirable parameter values, as shown in Table 5-1.

The next step is to perform a series of sensitivity studies to understand the individual influences of each and every parameter. It was observed by varying each parameter that some influence the results drastically, while others do not play a noticeable role. More interesting is the fact that some of the parameters have a unique influence on a different segment of the P-δ curve. For instance, the value s_0, the initial deformation resistance, has a significant control over the first 25% of the deformation curve. Higher the value of s_0, higher was the 'bump' in the initial part of the P-δ curve. Similarly, h_o values had a significant influence on the curvature of the P-δ curves. It was also observed that raising the value of h_o beyond a value of 1500 MPa did not produce significant changes to the response. The dimensionless exponents have a significant impact on the magnitude of the forces, especially parameter n. It also had a significant influence on the magnitude of force values at different strain rates. Other parameters were generally influencing each other in a complex manner, and hence their effects could not be isolated. The influence of the explained parameters has been demonstrated in Figure 5-3, with each parameter variation described by identical colored curves.

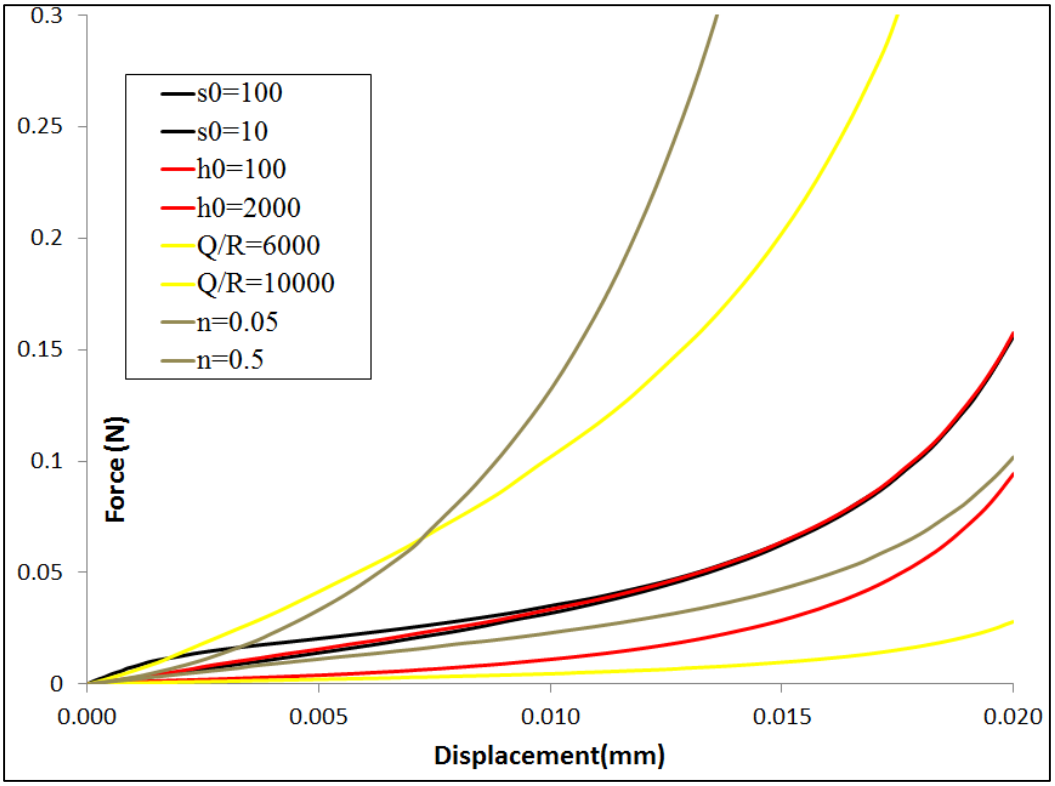

Figure 5-3. Effect of parmeters $s_0, h_0, Q/R$ and n on the force displacement curves. Increasing s_0 produces an initial bump in the curve. Raising h_0 beyond 1500 MPa has no significance. Increasing Q/R and n values increase the magnitude of forces.

The following steps involve choosing a parameter to be optimized and an appropriate algorithm for optimization. A potential objective function to minimize in this problem is the absolute area difference between the experimental and finite element P-δ curves. The second is to minimize sum of the square difference between the data points of the simulation and experimental P-δ curves. The choice of output function to minimize is now discussed. If the sum of squared difference between data points is chosen as the objective, then the differences between each and every data set for all the strain rate experiments have to be performed. Given the amount of experimental data, such an optimization problem might not be computationally inexpensive. Thus, the absolute area difference between the experimental and simulation curves was chosen as a parameter for optimization, though the sum of the squared distance was also monitored during the optimization. This also avoids the

need to perform interpolation of the forces at appropriate displacement data points where the forces are compared.

For the optimization algorithm, there are different classes of optimization codes based on the purpose and nature of the problem. Optimization techniques are broadly classified into three, gradient technique, direct search techniques and random search techniques. The gradient techniques require the function to be continuous and are expected to have first derivatives. They usually perform an excellent local optimization. Direct search techniques are more useful when the nature of the objective function to be optimized is unknown. It gives perturbation around the initial design point and seeks a pattern around the point. Random search techniques aim to identify a global optimum point and thus would incur high computational cost when the number of design variables is high.

Direct search methods are very useful in the case of engineering design, where the outputs might not be a algebraic functions of the input, and are prone to be non-smooth based on how the inputs influence each other. This method does not require a gradient, and hence does not settle on the local minima, but it helps in exploring the design space constrained by the upper and lower bounds. Hooke-Jeeves algorithm was thus chosen. This algorithm is a direct pattern searching method [46] which varies one design variable at a time with a step size and studies the change in the output variable. Hooke-Jeeves algorithm has been successfully implemented in optimization problems where the nature of the function to be optimized is not known, and had been used to arrive at material parameters by several researchers [46–48] .

The material parameters are to be calibrated with regards to three experimental strain rate data and the sufficiency of the obtained parameters are validated by its ability to predict the behavior under fourth strain rate, which was not used in the calibration. The upper and lower bounds of the design variables, which are the material parameter values, were deduced by sensitivity studies. The problem is a multi-objective, bound constrained optimization problem. It is multi-objective since three area differences between the curves of the experiment and simulation, for each strain rate, have to be minimized simultaneously. The flow diagram of the optimization set-up is shown in Figure 5-4. There are three closed circuits, each

circuit per strain rate. There are three components in each branch. Each circuit receives the input from the optimization module.

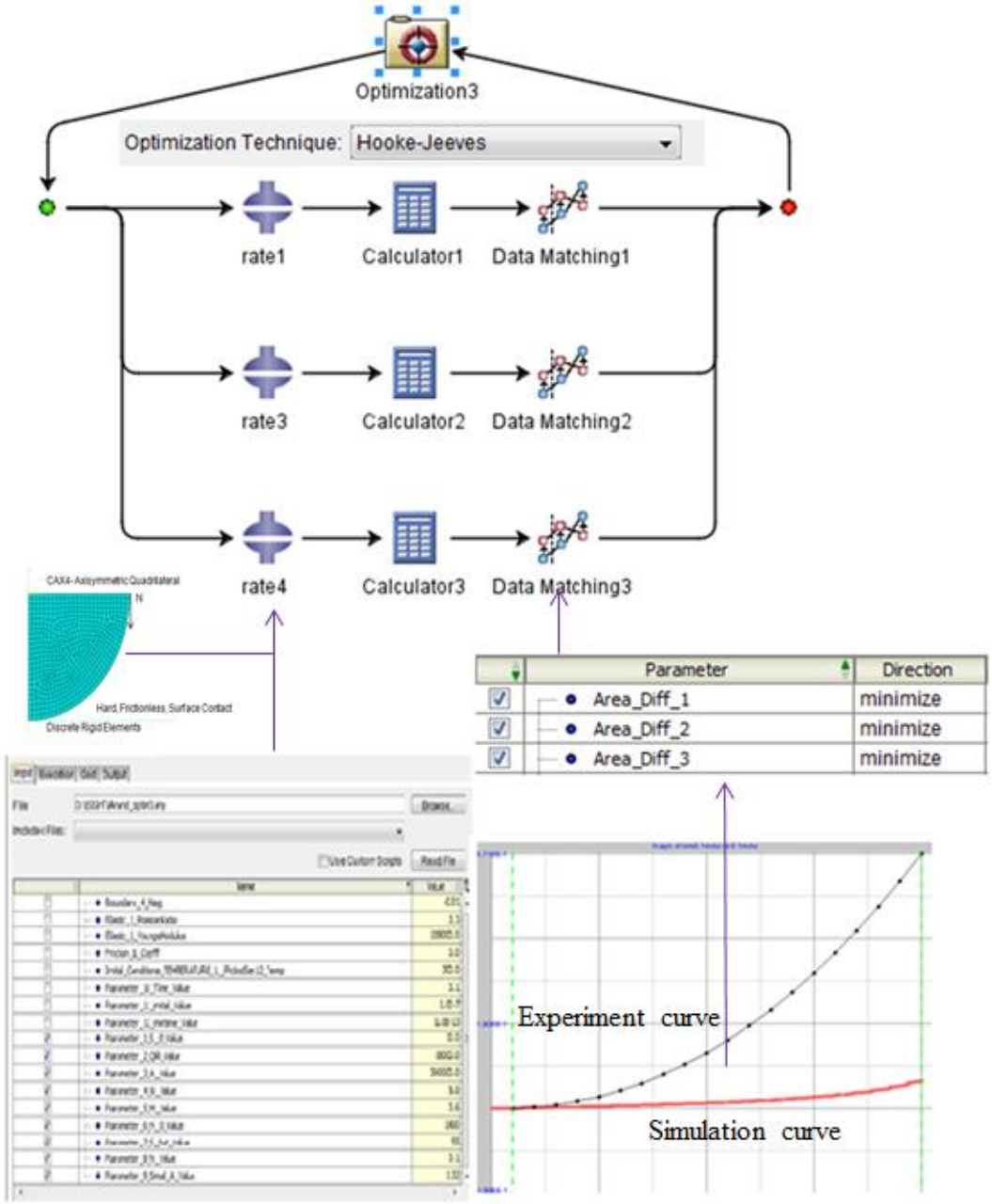

Figure 5-4. Automated procedure to arrive at the constitutive model parameters. Three out of four experimental data sets at different rates used for optimization. The optimization algorithm provides a set of parameters to each ring of the work-flow and area-difference between experiment and simulation P- δ are measured. The Hooke-Jeeves algorithm minimizes this area difference.

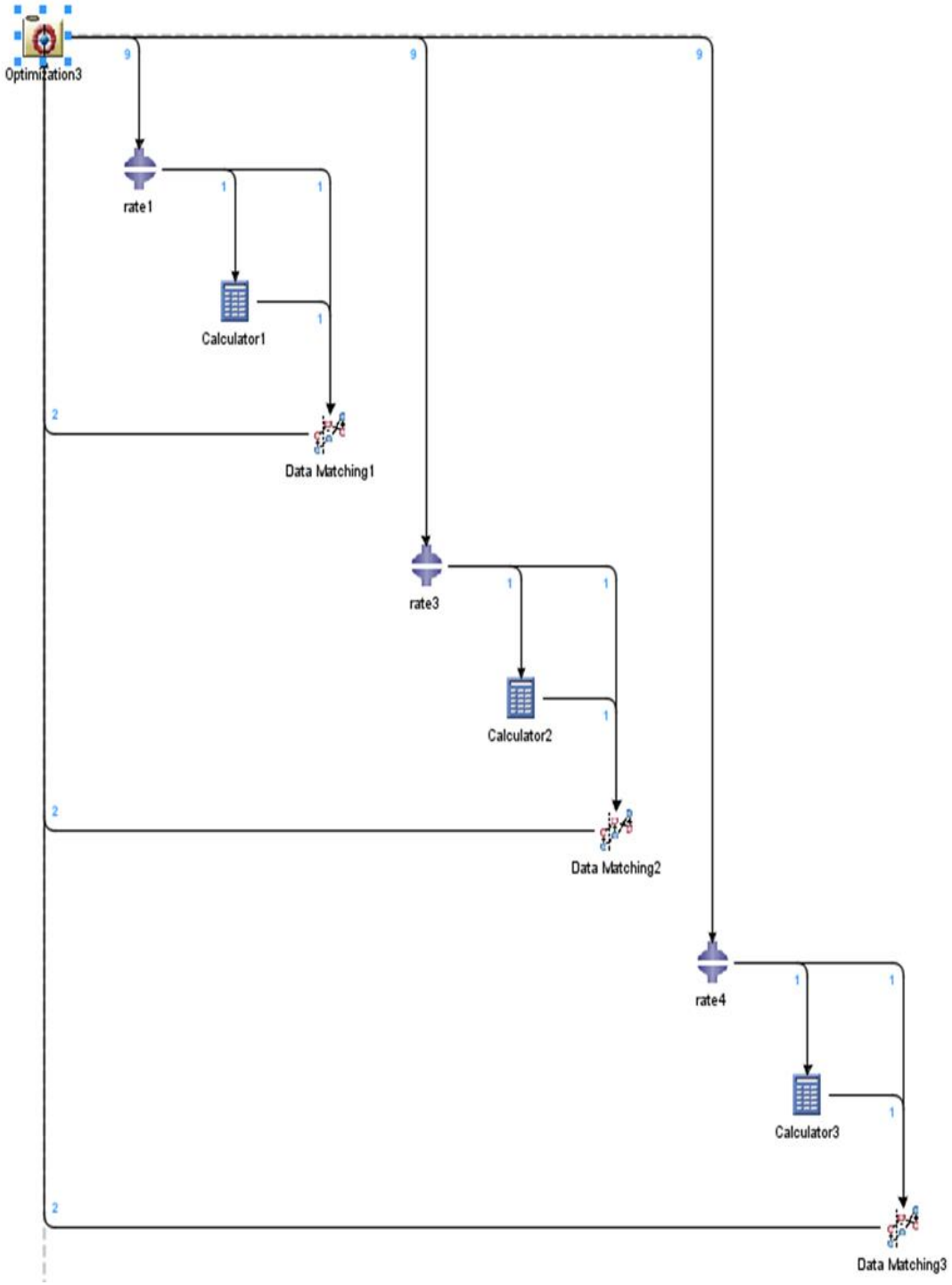

Figure 5-5. Nine parameters are provided as an input to finite element module and the data matching component returns two output functions, area difference between the curves and sum of squared differences. The area difference between simulation and experimental curves is used as an objective for minimization.

Each branch of the simulation flow has an ABAQUS component, a calculator and a data-matching component, and is executed simultaneously for the same material parameter input. The optimization process begins when the optimization components provide an initial set of parameters to each flow. The ABAQUS components receive the material parameters from the optimization module and would run the FE model with the given set of material parameters. The role of the calculator component is sign reversal of the displacement, which it receives from the ABAQUS component. Data matching component performs the task of estimating the area difference and data interpolation between the experimental and simulation P-δ curves. The data-flow between each component is shown in Figure 5-5. The optimization was carried out for several hundred runs and the task was repeated around the converged values to seek further refinement of the material parameters. The parameters obtained through this method are shown in Table 5-2. The P-δ curve predicted by these parameters against one set of experimental values are shown in Figure 5-6. It could be verified that the parameters successfully predicted the experimental behavior at rate of 0.1 mm/min, which is the experimental data not used for calibration.

Table 5-1. Upper and lower bounds set for the material parameter optimization based on sensitivity studies.

Parameter	Lower bound	Initial Value	Upper bound
s_0	8	9	12
A	3E4	3E6	3E8
$\hat{s}$	50	65	100
Q/R	7000	8200	9000
a	1	1.2	1.5
m	0.2	0.5	1
n	0.08	0.15	0.2
ξ	6	7	15
h_0	1000	1200	1500

Table 5-2. Optimized set of parameters to explain the behavior of FAB at low and intermediate strain rates.

s_0 (MPa)	A (s^{-1})	$\hat{s}$ (MPa)	Q/R (K)	a	m	n	ξ	h_0 (MPa)
10.72	3E5	55	8000	1.32	0.6	0.1	8	1400

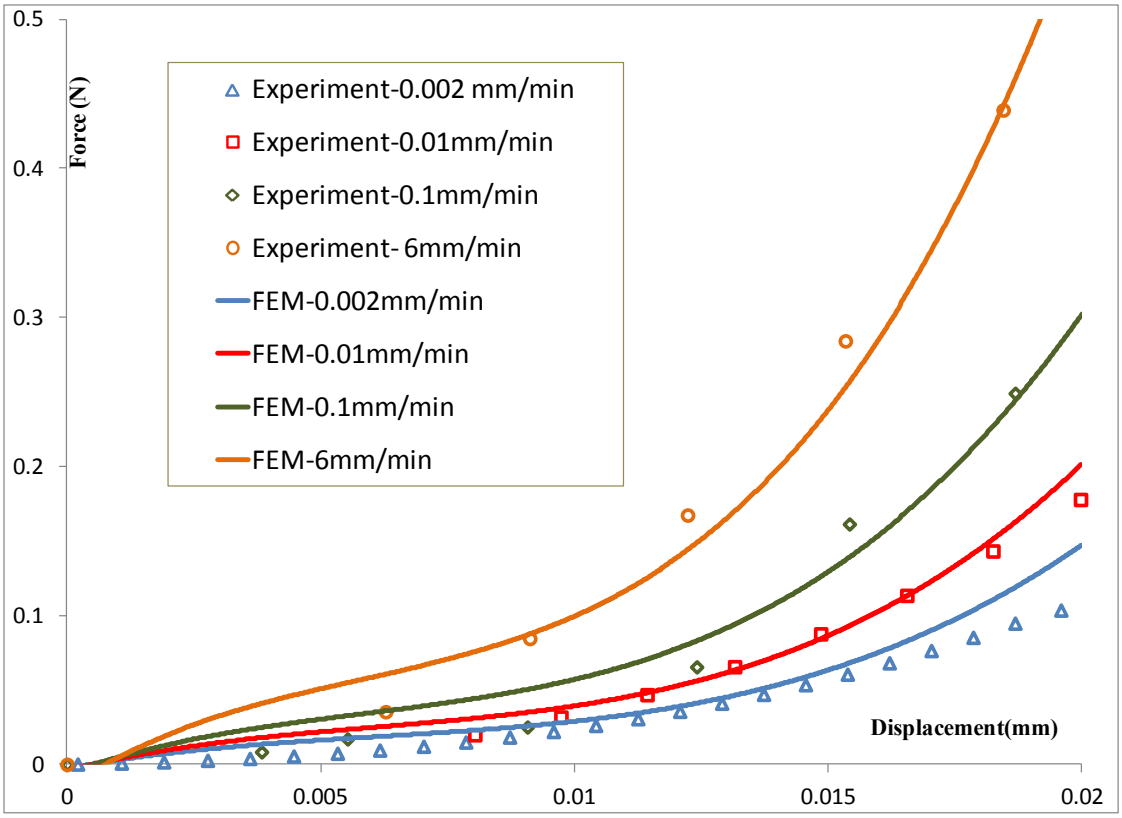

Figure 5-6. Correlation between experimental data and plot produced by finite element analysis. Optimal parameter values in Table 5-2 successfully explained the behavior at all strain rates, including the data set which was not used for optimization (0.1 mm/min).

Optimization runs were also performed with the experimental data from three lower loading rates, and were checked against the ability to predict the behavior at 6 mm/min. The values obtained using this method are shown in Table 5-3 and the correlation with experimental data are shown in Figure 5-7.

Table 5-3. Table of optimized material parameters obtained using low strain rates.

s_0 (MPa)	A (s^{-1})	$\hat{s}$ (MPa)	Q/R (K)	a	m	n	ξ	h_0 (MPa)
10.72	566312.5	55	7600	1.5	0.505	0.205	9.9	1500

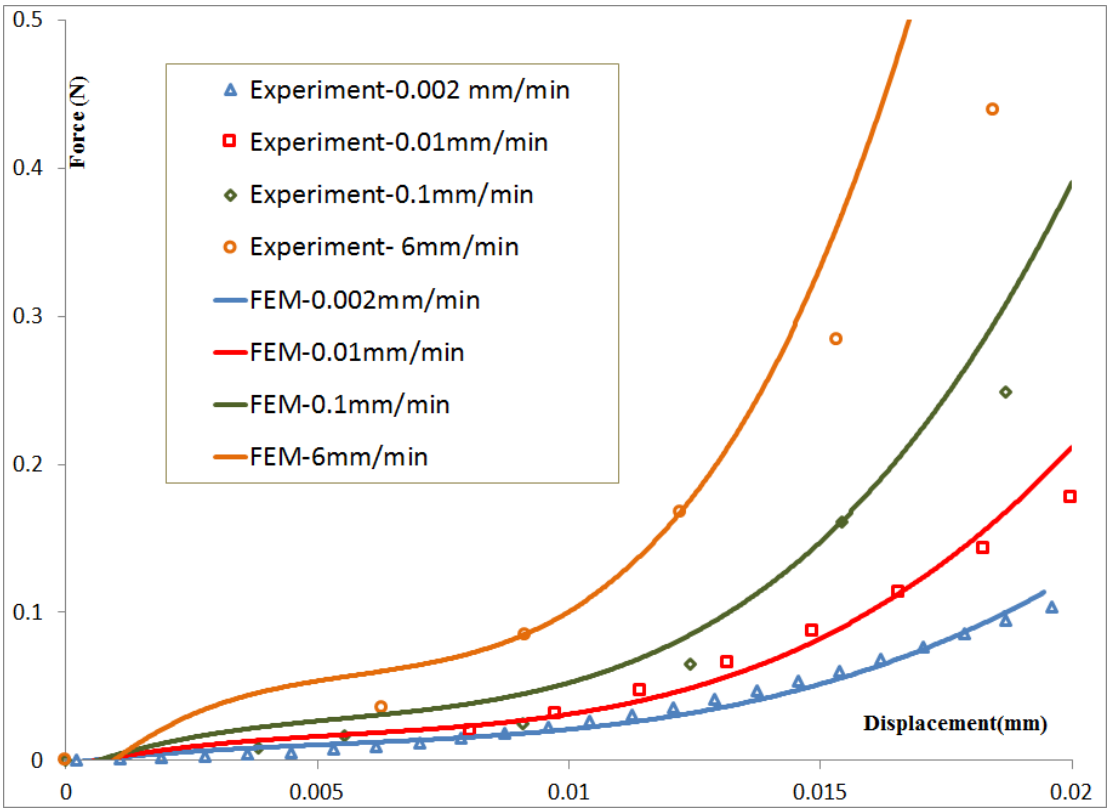

Figure 5-7. Correlation between experimental data and plot produced by finite element analysis. Optimal parameter values in Table 5-3 does not effectively capture the behavior at a high loading rate (6 mm/min) effectively.

Since high strain rate behavior is of more interest during the wire bonding process, parameters shown in Table 5-2 which explain that behavior better, have been adopted hereafter. Though one set of parameters has been successfully used to represent the behavior at various strain rates, it is also essential that these parameters explain the behavior at different temperatures. To include the ability of the model to predict the behavior at higher temperature, a 'modified' Anand model is adopted in the next section.

5.6 Modified Anand Model

Work by [49–51] has suggested that Anand model is not sufficient to cover the entire strain-rate and temperature dependent behavior of the solder material. Thus, a modified Anand model [53] is adopted to introduce additional parameters to account for the strain rate and temperature sensitivity. The additional parameters in themselves are seldom of any physical significance, but are merely a mathematical manipulation of the pre-existing physical parameters so that it would explain the observed response better.

In modified Anand model, two of the actual model parameters are expressed as a function of temperature and strain rate. The initial deformation resistance s_0 and the hardening coefficient h_0 are expressed in the following manner.

$$s_0 = s_1 + s_2 T + s_3 T^2 \tag{50}$$

$$h_0 = A_0 + A_1 T + A_2 T^2 + A_3 \dot{\varepsilon}_p + A_4 \dot{\varepsilon}_p^2 \tag{51}$$

Thus, there are additional six parameters that will allow us to fit the temperature dependent data. The functionality is available in ABAQUS/Standard and is defined in a similar fashion as the original Anand model, but the two lines following the keyword *CREEP are to read as follows

s_1, Q/R, A, ξ, m, A_0, $\hat{s}$, n

a, s_2, s_3, A_1, A_2, A_3, A_4

T_0, the reference temperature is an added parameter at the end of the second line for versions earlier than 6.14, as discussed in the earlier sections.

To fit these parameters, a similar procedure outlined for the Anand model was used, and the equations (50) and (51) were provided as constraint equations so that the value of s_0 and h_0 are not altered or mildly altered, if at all. However, a simpler solution procedure is described in the following section, deducing parameters of significance and their fitting procedure.

5.7 Solution to Modified Anand Model as a System of Linear Equations

It is established from the sensitivity studies that the parameter s_0 only influences the initial part of the *P-δ* curve, causing a ' bump' in the force value. Such a feature was not observed in the experimental response, and thus s_0 was kept at a minimum. The influence of s_0 was not strong in the high temperature tests. Raising the value of s_0 as a function of temperature is thus not necessary, and thus s_2 and s_3 were set to a value of zero. Value of s_1 is the same s_0.

The strain rate sensitivity of the experiments have been sufficiently captured by the values of h_0 earlier, thus strain dependent coefficients A_3 and A_4 are set to zero in Equation (51). Instead of optimizing for the remaining coefficients of h_0 with an additional constraint equation, it was computationally efficient to optimize for three h_0 values at three different temperatures individually, and solve Equation (51) as a system of linear equations with three unknowns for each temperature.

The individual values for h_0 were estimated as 800 Mpa and 600 Mpa at 348 K and 373 K respectively. At 300 K, the value of h_0 was found as 1400 MPa in the previous section. The corresponding values of A_0, A_1, and A_2 by solving Equation (51) are shown in Table 5-4.

These coefficients can then be used to predict experimental data at 323 K, which was previously not used for fitting. The model's ability to predict the behavior is demonstrated in Figure 5-8.

Table 5-4. Modified Anand model parameters obtained as a solution to system of linear equations.

A_0	A_1	A_2
11586	-52.4452	0.0616

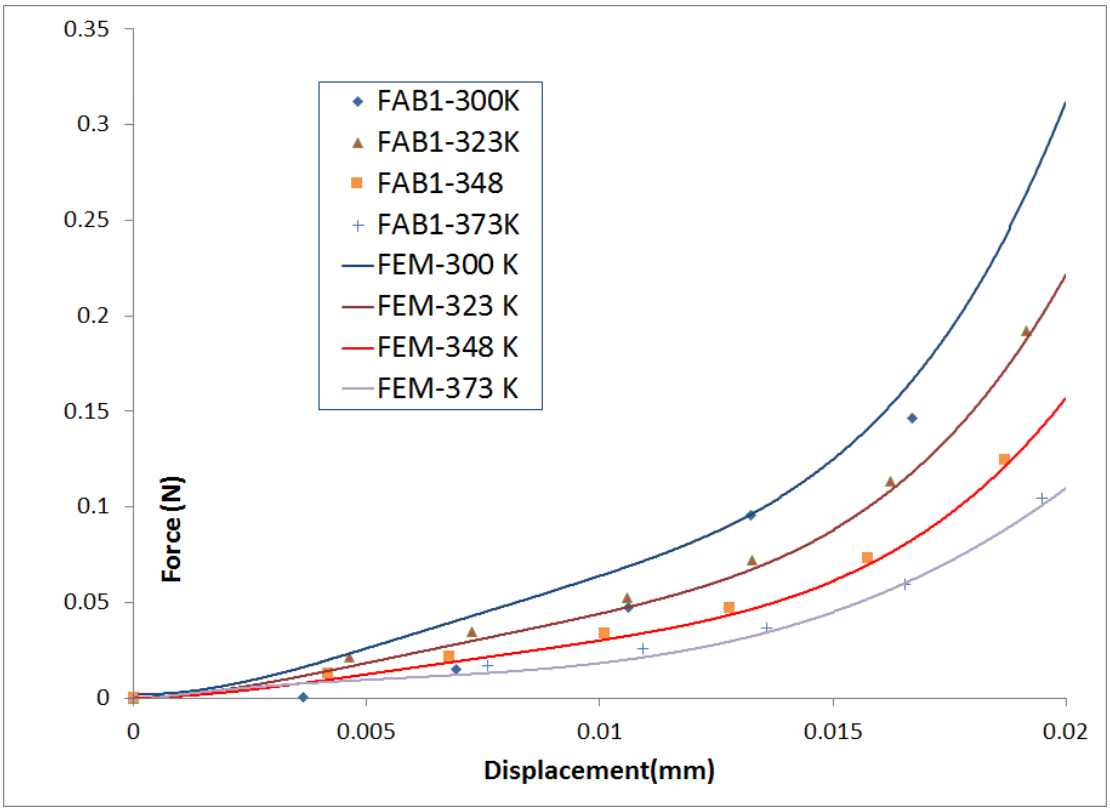

Figure 5-8. Correlation between experimental data and plot produced by finite element analysis. The optimized parameters for modified Anand model successfully described the behavior at all strain rates and temperatures, including the data set that was not used during optimization (323 K).

In summary, various viscoplastic models were discussed and an appropriate model was selected for the characterization of the free-air ball. An inverse finite element model was constructed and the influence of each Anand model parameter on the *P*-δ response was studied. An automated, bound constrained optimization problem was posed where the material parameters were iterated till the FE response matched the experimentally observed response at low and intermediate strain rates through a range of temperatures. In the subsequent chapter, these material models are used to model wire bonding process, and estimate the risk of fracture in the ILD.

CHAPTER 6. FINITE ELEMENT MODELING OF CU WIRE BONDING

6.1 Overview

In this chapter, an implicit finite element model of the wire bonding process is constructed in ABAQUS/Standard using the "*VISCO" step to accommodate transient response of the FAB with time-dependent material properties. The Anand constitutive model parameters estimated in the previous chapter are used to model the FAB during the wire bonding process. The procedure for the construction of the model are elaborated and different parameters of interest, such as deformation of the FAB, stresses in the bond pad, structure under pad (SUP), and contact parameters between the bond pad and the FAB are studied. These parameters are in turn compared with the explicit wire bonding model described in reference [2], which uses rate-dependent properties of bulk copper instead of experimentally characterized FAB properties. Two critical stages of wire bonding, namely, the impact and ultrasonic vibration stages, as well as the bonding of the FAB to the bond pad is simulated. This "macroscale" model provides critical stress locations on the die during wire bonding. The deformations are then transferred as boundary conditions for the local model.

Relative to the attempts to simulate the process of gold wire bonding, the literature on simulating copper ultrasonic wire bonding is relatively few [11, 54]. Moreover, the existing simulations use rate dependent material properties of copper [2] that may not reflect the behavior of the FAB. As mentioned in the previous chapters, the behavior of the FAB can be significantly different, since they are formed by the process of electronic flame-off. FAB are softer than copper due to significant grain orientation changes during their formation [13]. Thus, using the experimentally measured characteristics of the FAB into models for the process of wire bonding is a significant step towards accurately predicting the deformation and risk of failure during the wire bonding process. A transient model is thus constructed in

ABAQUS/Standard (i.e., the implicit version of the software) using the Anand model parameters for the FAB. Though an explicit finite element model is more appropriate to model the large deformation during the wire bonding process, given the short time duration of the bonding process, the Anand viscoplastic model is not readily usable with the explicit version of the ABAQUS finite element software at the current time. Different contact conditions adopted during the impact and the bonding of the FAB to the bond pad is elaborated. Solution methodologies to obtain a converged solution are discussed. Real phenomena such as pad splash and pad lift are captured by the finite element model and discussed.

6.2 Wire Bonding Modeling Parameters

The following bonding process parameters from reference [2] was used to construct the geometry of the finite element model. The parameters defined are shown in Figure 6-1

Table 6-1. Dimensions used in finite element modeling [2].

Parameter	Value
Bond Pad Opening (BPO)	28 μm
Bond Pad Thickness (BPT)	1 μm
Mashed Ball Diameter (MBD)	27 μm
Bonded Ball Height (BBH)	6 μm
Wire Diameter (WD)	15 μm
Hole Diameter (H)	19 μm
Tip Diameter (T)	45 μm
Chamfer Diameter (CD)	23 μm
Inner Chamfer Angle (ICA)	90°
Face Angle (FA)	11°
Outside Radius (OR)	6 μm

The FAB diameter for the process is given by the following empirical formula

$$D_{FAB} = 1.5H^2(H - WD) + (CD^3 - H^3)/4\tan(0.5CA) + 1.5MBD^2 \text{x} BBH \quad (52)$$

The process is simulated using a finite element model containing three parts namely, the capillary, FAB and dies assembly, and that exploits half-symmetry. The capillary is represented by a rigid surface, extracted from the inner surfaces of the three dimensional capillary that smashes the FAB against the bond pad. A reference point is created on the rigid surface of the capillary and the boundary conditions for the impact and vibration stages are prescribed at this point. This point also corresponds to the point of attachment of the horn in the bonding equipment, which applies the ultrasonic excitation.

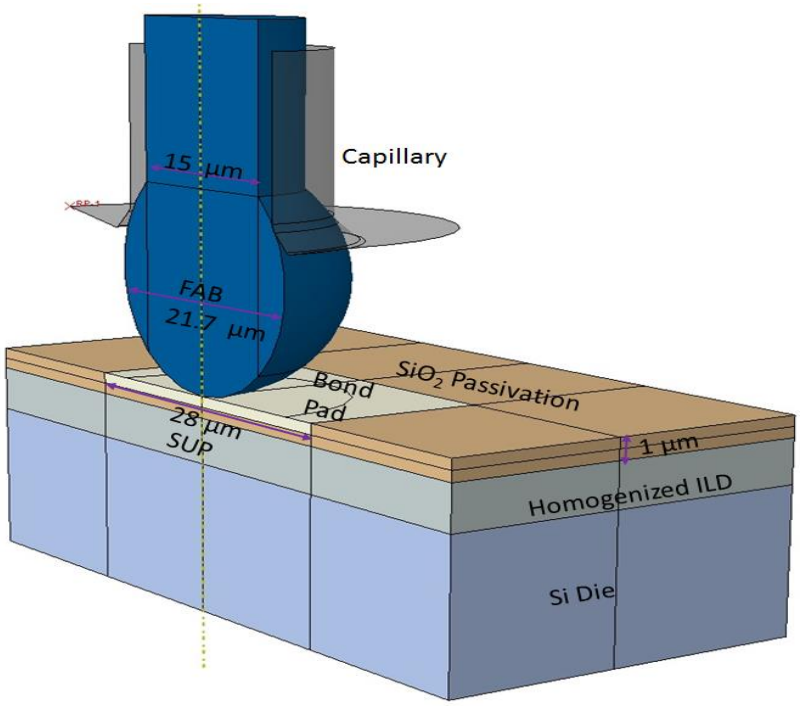

Figure 6-1. Finite element model with dimensions. Parts with different material properties are colored differently.

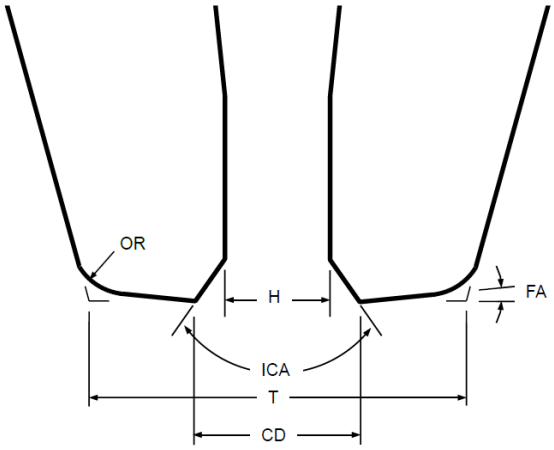

Figure 6-2. Capillary dimensions for the developed wire bond model. Inner surfaces of this part are modeled as a rigid surface.

Using Equation (52) , the dimension of the FAB for the given configuration is calculated as 21.7 μm. An initial node to node contact is established between the FAB and bond pad and small initial clearance is maintained between the FAB and the capillary.

6.3 Material Properties and Meshing

Given the high temperature and strain rates at which the bonding process is carried out, appropriate strain rate dependent material models must be used in order to capture the magnitude of stresses accurately in the simulation. For the Cu FAB, Anand viscoplastic model with the parameters extracted in the previous chapter was used. The bond pad is made of aluminum and elasto-plastic material models from reference [2] was used for this material. ILD layer of the die stack includes different materials in addition to the copper signal lines and vias. But at the macroscale, the ILD stack is modeled as a homogenized layer with averaged material properties. The details of the ILD stack structure is included while simulating fracture in the 'local' model. Elastic constitutive models have been used to represent the brittle dielectric materials. The material properties are shown in the Table 6-2 below.

Table 6-2. Material properties used in finite element analysis [2].

Part	Material	Young's Modulus (GPa)	Poison's Ratio	Yield Strength (GPa)	Tangent Modulus (GPa)
Pad	Aluminum	61	0.3	218	100
Die	Silicon	130.5	0.28	-	-
ILD	Homogenized	81	0.26	-	-
Passivation	SiO_2	73	0.17	-	-

Partitions were created on the geometry to create a mesh with hexagonal elements. The FAB and the die pad assembly were meshed using C3D8R, 8-noded linear brick element with reduced integration and hourglass control. The rigid capillary surface was meshed with rigid R3D4 bilinear rigid quadrilateral elements.

6.4 Boundary Conditions

The model requires step dependent boundary conditions. The model has two kinds of elements, solid elements and shell elements. Solid elements have three translational degrees of freedom, whereas shell elements have three additional rotational degrees of freedom. The displacements along the X, Y and Z directions are denoted here as U1, U2 and U3 respectively. The boundary conditions that are common to both impact and ultrasonic excitation stages are applied at the initial step. In this step, symmetry conditions are prescribed on the faces of FAB and the die assembly shown in the Figure 6-3, and the U3 degrees of freedom of the bottom face of the die assembly is fixed. On the faces orthogonal to this bottom face the U1 and U2 degrees of freedom are arrested. A bond temperature of 473 K is applied to the FAB and the die assembly as a predefined temperature field in the initial step. These boundary conditions and temperature are automatically propagated through the rest of the steps that follow the initial step.

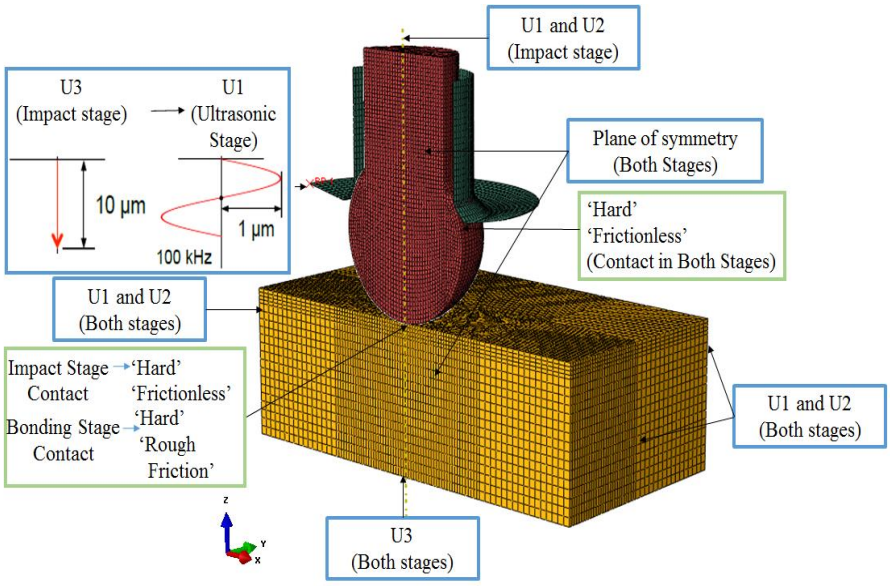

Figure 6-3. A meshed finite element model indicating the boundary conditions and contact definitions at initial, impact and ultrasonic vibration stages.

The impact step follows the initial step. A displacement condition U3 of 10 µm was applied on the rigid point of the capillary, and the step lasted for a period of 1 µs, simulating an impact velocity of 10 m/s. The remaining five degrees of freedom of the rigid point were arrested. The central axis of the FAB was constrained along the U1 and U2 directions. Following the impact step was the ultrasonic vibration step, where the boundary conditions applied during the impact stage were disabled. A displacement U1 of 1 µm was applied on the rigid point during the ultrasonic vibration step, with a frequency of 100 kHz, for a step time of 1 µs, and the rigid point was constrained in all the other degrees of freedom.

6.5 Contact Definitions

To study the interaction between the capillary surface, FAB and bond pad, step-dependent contact formulation, discretization and enforcement were defined. A finite sliding contact formulation was adopted for all the surfaces, with surface to surface contact discretization. In such a discretization, the contact is enforced over the slave surface in an average sense, and is helpful in reducing nodal penetration of the rigid surface over a 'soft' slave surface [55].

During both the stages, a “hard” contact surface interaction behavior without separation was used to define contact between all the surfaces in the normal contact direction. A direct enforcement of such a contact was adopted. Such an enforcement depends on pressure-penetration curve, where, as soon as the contact is established, the pressure “strictly” rises to the contact pressure through Lagrange multipliers [55]. In the tangential direction, frictionless contact was assumed at the impact stage, since a friction coefficient results in non-symmetrical stiffness matrices, which are computationally expensive to solve, especially because of the viscoplastic behavior of the FAB.

During the ultrasonic bonding stage, however, frictional properties are necessary to simulate bonding between FAB and the bond pad in the die assembly. Thus, the friction between FAB and bond pad was modified to “rough friction” in this stage. It corresponds to an infinite coefficient of friction enforced using the Lagrange multiplier method described earlier. In such a contact, no slip is allowed between the nodes, and they remain bonded as soon as they come in contact. Such a condition is often used with no-separation normal contact to avoid convergence issues. The bonded condition would simulate a conformal deformation of the FAB and bond pad, and would represent the most severe deformation that would occur during wire bonding. The option of “Discontinuous Analysis” was enabled in order to increase the number of equilibrium and severe discontinuity iterations and to avoid any premature cut-back in increments of time.

6.6 Results and Discussion

6.6.1 FAB Deformation

The Cu FAB is collapsed on the bond pad by the downward motion of the capillary. Plots shown in this section correspond to the end of impact stage and at the peak amplitudes of ultrasonic excitation. The Von Mises stress contours are shown in Figure 6-4 (a) and (b). The contact pressure between the FAB and the capillary is the major cause of these stresses. The stress value is approximately the same around the contact area during both the stages and the high stress area gradually migrates towards the interface between die pad and the passivation. A peak value of 620 MPa

was noted in the FAB, which is 35% higher than that of Au FAB on Aluminum pad as described in reference [56]. It can also be observed that during the ultrasonic stage, the bond pad undergoes conformal deformation along with the FAB.

6.6.2 Pad Splash

When the ball is impacted and bonded on to the pad, the pad is gradually pushed out from the bonding zone. This phenomenon is referred to as pad splash and was captured in the simulation. The pad splash (described by the contours of U1) at the end of impact stage and peak excitations of vibration stages are shown in Figure 6-6.

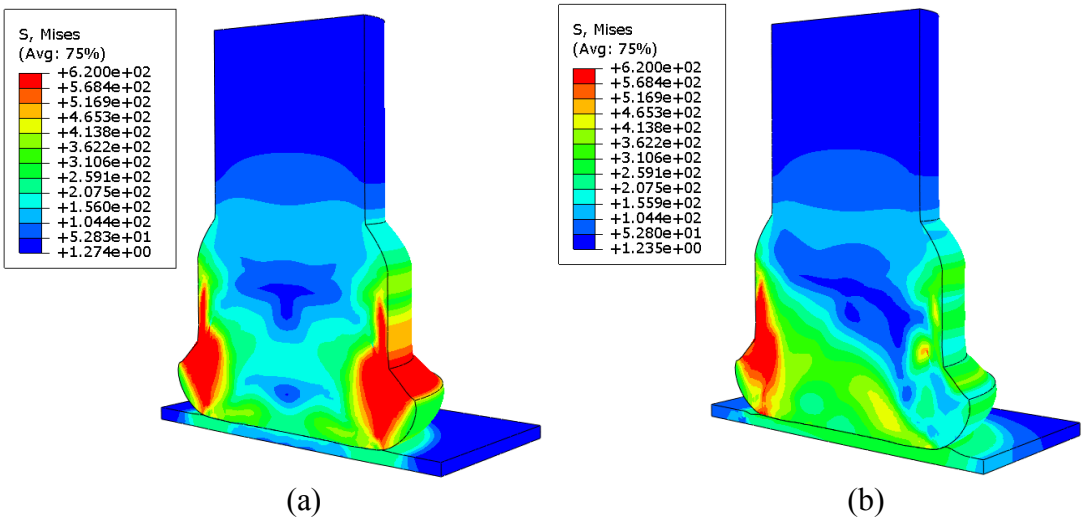

Figure 6-4. (a) Mises stress at the end of impact stage (b) Mises stress at the first peak excitation of ultrasonic stage.

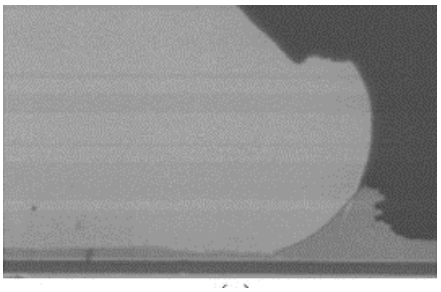

Figure 6-5. Al pad being squeezed during wire bonding [11].

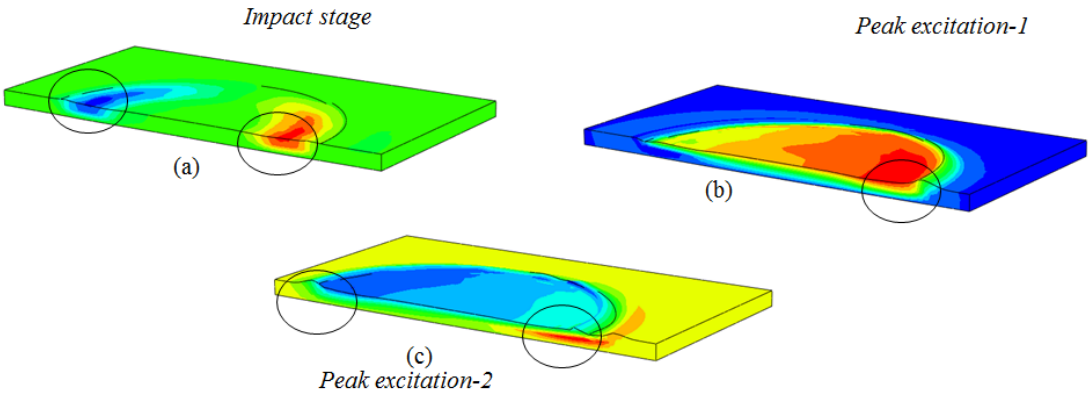

Figure 6-6. Pad splash captured at the end of (a) Impact stage (b) First peak excitation of ultrasonic stage (c) Second peak excitation of ultrasonic stage.

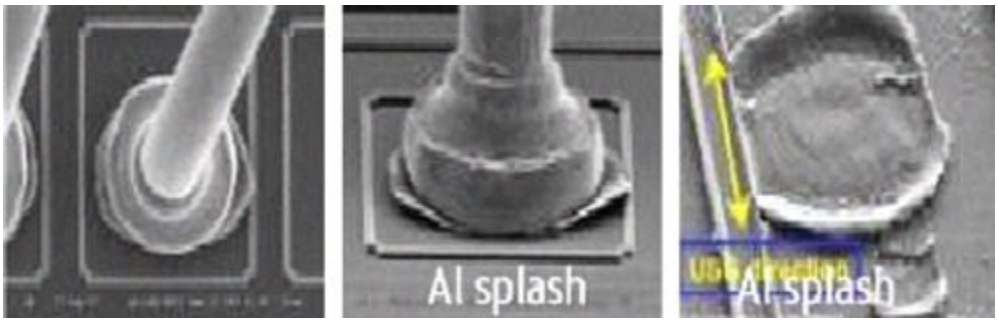

Figure 6-7. Al pad splash after ultrasonic bonding [11].

6.6.3 Evolution of Contact Pressure at Bond Pad-FAB Interface

The contour of contact pressure at different time steps, *T*, is shown in Figure 6-8. During the initial steps, the contact pressure decays from the center to the contact periphery similar to the pressure profile assumed in Hertz contact, as discussed in Chapter 4. However, as the contact area increases, the contact pressure concentrates towards the periphery, forming a ring of high pressure distribution. Such a behavior can be attributed to the non-uniform pressure distribution occurring due to the compressive loads applied at the tip of capillary.

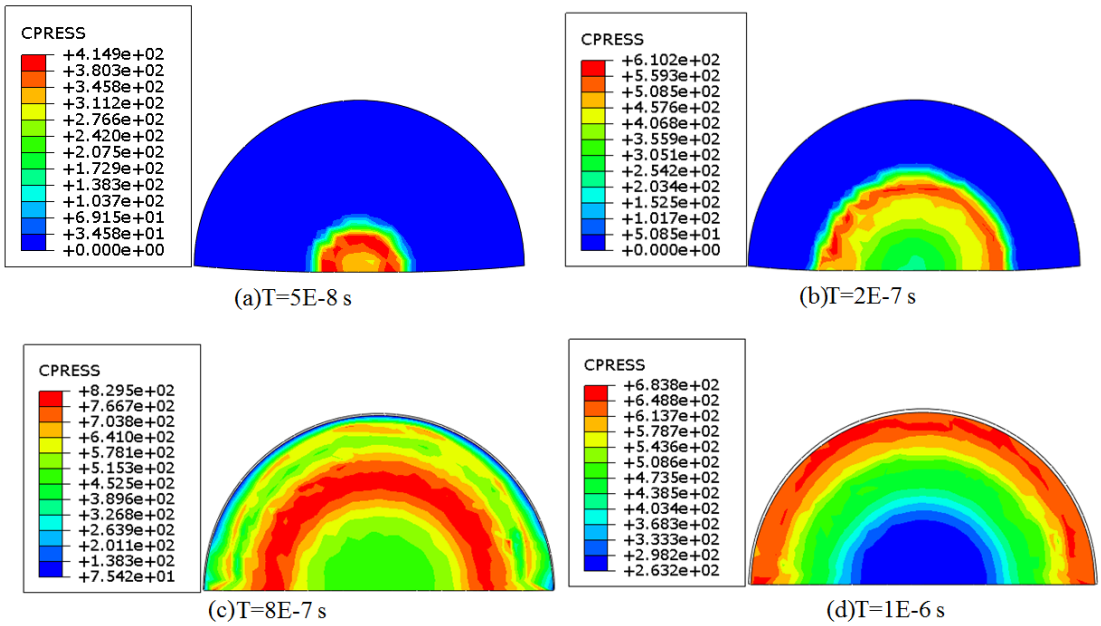

Figure 6-8. Contact pressure at the interface between FAB and the bond pad during impact stage at time steps (a) T=5E-8 s (b) T=2E-7 s (c) T=8E-7 s (d) 1E-6 s.

During the ultrasonic stages, the contact pressure is initially high at the start of the bonding, but as the bonding area increases, it evenly distributes itself as shown by the contour plot at different time steps *t*, in Figure 6-9.

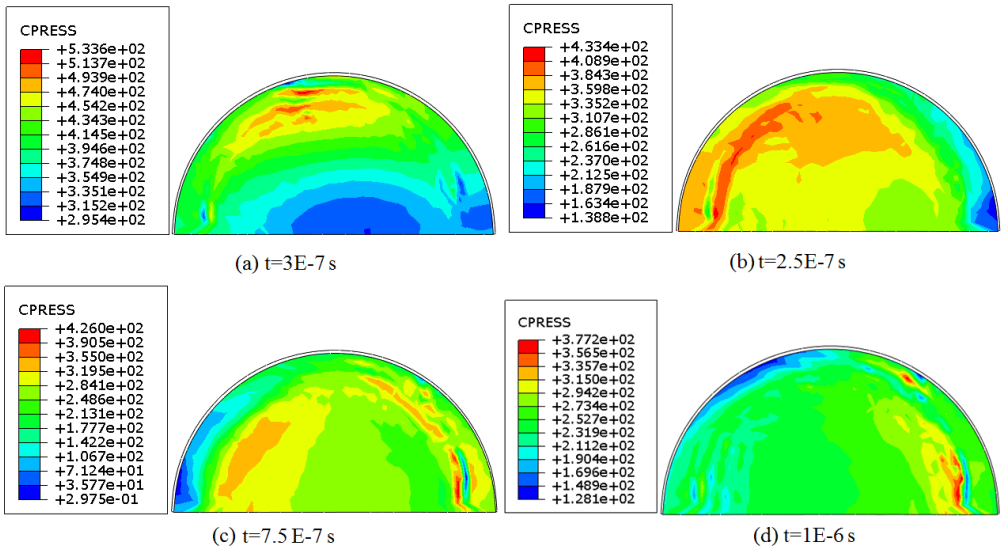

Figure 6-9. Contact pressure at the interface between FAB and the bond pad during ultrasonic stage at time steps (a) t=3E-7 s (b) t=2.5E-7 s (c) t=7.5E-7 s (d) t=1E-6 s.

6.6.4 Stresses in Structure under Pad

The Structure under pad (SUP) is the section of the ILD that lies directly underneath the bond pad of the dielectric assembly. The Z-direction sress, referred hereon as S33, is often the main driving force for ILD fracture [15,53]. Thus the stresses in the direction of impact are studied in the SUP, and are compared with the results obtained in reference [2] using rate dependent properties of bulk copper. The contour of S33 at the end of impact step is shown in Figure 6-10 (a) and (b). It can be concluded that the viscoplastic behavior of FAB developed in the present study predicts a lower value of stresses in the SUP. Consequently, the deformations are smaller in comparison, and these deformations are to be provided as boundary conditions for the 'local' isogeometric model.

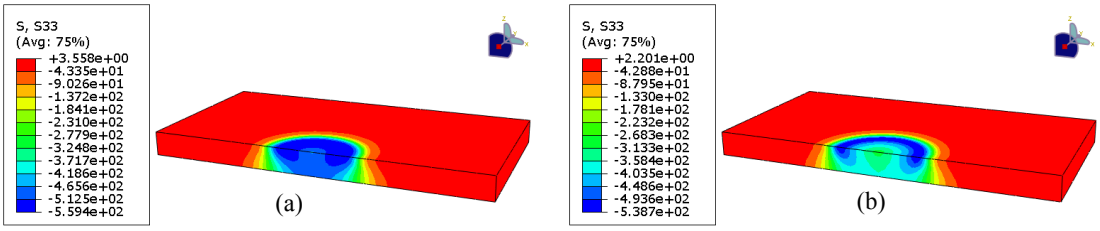

Figure 6-10. The stresses in the Z-direction on the ILD compared between (a) Material properties used in reference [2] (b) Viscoplastic material properties characterized in this study.

6.6.5 Pad Lift-off

At the peak excitations of the ultrasonic stages occurring at t=2.5 E-7 s and t=7.5 E-7 s, the bond pad undergoes conformal deformation but tries to fracture the SUP, by exerting tensile forces on it. This phenomenon is termed as 'pad lift-off' and has been captured in the simulations.

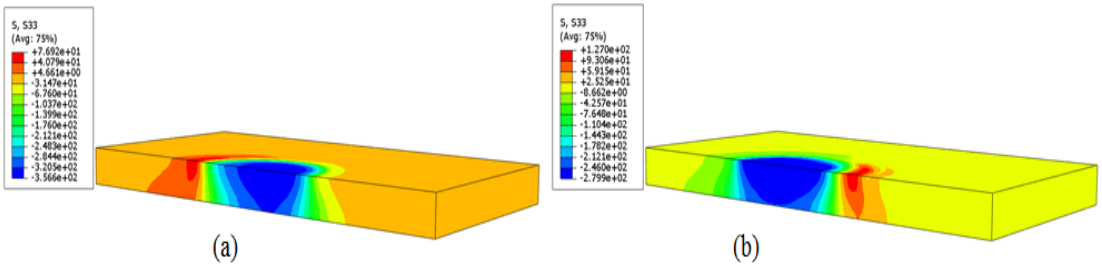

Figure 6-11. The stresses in the Z-direction on the ILD at (a) First peak excitation of the ultrasonic stage (b) Second peak excitation of the ultrasonic stage.

In summary, an implicit model of the wire bonding process was constructed, incorporating the modified Anand model parameters, which were obtained in the previous chapter. A half-symmetry finite element model was constructed to model two severe stages of the wire bonding process, the impact stage and the ultrasonic excitation stage. The 'macroscale' modeling of the multi-modeling step was helpful in describing stresses in the SUP, contact pressure on the pad, and bonding of FAB to the bond pad. It was concluded that using the constitutive behavior measured from FAB yields lower stress and deformation values than when using elasto-plastic properties of bulk copper. The deformations of the SUP from this stage are provided as an input for the local, isogeometric model, which helps in understanding the sites of potential fracture.

CHAPTER 7. SIMULATIONS OF FRACTURE IN ILD STACKS

7.1 Overview

The mechanical integrity of the ILD stacks is an important reliability consideration, especially for the porous low-k and ULK dies. In such dies, fracture is a risk, not only at the interfaces of the dielectric, but within the bulk dielectric material as well. Driving forces of such fractures have been attributed to many factors, such as, forces involved in wire bonding, stresses during fabrication, mismatch in coefficient of thermal expansion, etc. The main challenge to simulating such failures is the availability of a computationally effective framework that is capable of nucleating and propagating the cracks [17]. Though studies exist in literature involving the use of cohesive zone elements to propagate the crack, such a procedure usually requires one to populate the potential crack path with CZM elements, and thus assume crack paths apriori. References [57–59] have studied crack propagation paths based on methodologies such as XFEM, however, studies that identify the potential points of crack nucleation are uncommon. Such simulations are essential for the development of crack arrest features in dies [1].

One of the major pitfalls of Linear Elastic Fracture Mechanics (LEFM) is the inability to predict crack nucleation. LEFM assumes the presence of a pre-existing crack of a finite length. To overcome this limitation, a cohesive damage description and a novel simulation methodology based on isogeometric approximation [18] is adopted in this chapter. An accumulated damage parameter is calculated and is used to analyze the risk of fracture in ULK dies. Using this tool, two objectives of interest, the potential sites of crack nucleation and the likely paths of crack propagation are studied.

7.2 Modeling Methodologies

To simulate the nucleation of crack, isogeometric enriched field approximations are used. Geometrically speaking, cracks and interfaces are lower-dimensional features in comparison with the two dimensional or three dimensional structure in which they are present [18]. On these lower-dimensional features, two kinds of discontinuities exist. The first is the material discontinuity across such features, as encountered during the problem of material phase evolution. The second is the discontinuity in behavior such as a jump in the displacement across a crack. The methodologies available to capture the behavior of such interfaces can be classified into two, geometrically speaking. First, are the explicit schemes in which the lower-order features have geometric properties such as the existence of normals or curvatures [18]. Implicit schemes are those in which such geometric properties of the interfaces are not directly computable. Now, based on behavior, two possible classifications of the interface are possible. In behaviorally explicit methodologies, the interfaces are represented as an internal boundary that requires a discretization of the domain to conform to the crack or the interface. In behaviorally implicit schemes, the approximations of the interfaces are used to enrich the underlying geometry.

Finite element method (FEM) is a geometrically and behaviorally explicit scheme in which the mesh conforms to representation of the interface. However, as the interface evolves, re-meshing is required. Refining the mesh near the interface makes the technique computationally expensive. The accuracy of the solution is also largely dependent on the refinement of the mesh and thus is an important limitation of the method.

There also exist schemes that use a geometrically implicit, but behaviorally explicit strategy. In this methodology, an assumption is made that the behavior of the interface is known beforehand. Methodologies such as PUFEM [60,61] use the prior knowledge of the interfacial behavior to enrich the behavior of the underlying domain. This method was later combined with FEM by references [62,63], where additional degrees of freedom were added to the nodes to represent the known local behavior at the interfaces. The eXtended finite element methods (XFEM) proposed in reference [64], that belongs to the above class of methods, attempts to describe the crack

independent of the underlying mesh. A Heaviside step function is used to model the displacement jump across the crack. One disadvantage of the method is the need for tracking of the nodes influenced by the crack. Recently, implicitized level-sets are used together with the XFEM method to eliminate the crack-mesh interaction problem [64]. However, the introduction of the level sets increases the degrees of freedom and the tracking of level sets further increases the computational cost [18].

7.3 Approximations of Geometry and Behavior

In the present study, a geometrically explicit and behaviorally implicit methodology developed by Tambat and Subbarayan [18] was adopted to simulate the damage of ILD stacks. The advantage of the method is the ability to maintain the geometric exactness of the stacks, and the ability to enrich the underlying domain with behavior on interfaces that are as low as 10 nm thick. For a mesh to span micro meter to nano meter length scales would be computationally expensive.

In this methodology, the ILD stacks are constructed as a global approximation where primitive geometries are hierarchically composed to form a complex geometry as shown in Figure 7-1[1] .

The geometric domain and behavior field are represented by the parametric mapping defined as $V_\Omega(\xi,\eta,\zeta)\to x$ and $f_\Omega(\xi,\eta,\zeta)\to u$. The lower-order enriching geometry and field are defined as $C_\Gamma(s,t)$ and $f_\Gamma(s,t)$ respectively. In the above representations, Ω represents the geometric domain and Γ represents the boundary. *V* and *C* represent tri-variate and bi-variate geometry, respectively.

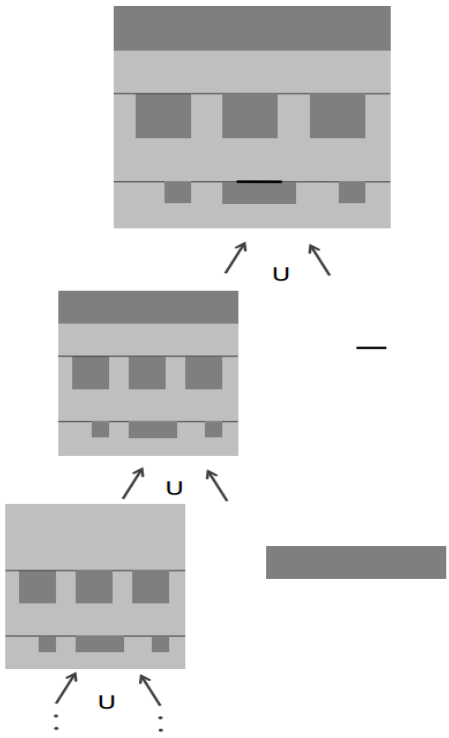

Figure 7-1. Construction of the approximation by composing lower order primitives[1].

The hierarchical composition can be mathematically represented as [1]

$$f(x) = w_{\Omega} f_{\Omega}(x(\xi,\eta,\varsigma)) + w_{\Omega}^{e} f_{\Gamma}^{e}(x \to (s,t)) \tag{53}$$

Where w is a weight function. The weight functions must obey the partition of unity property [17]:

$$w_{\Omega} + w_{\Omega}^{e} = 1 \tag{54}$$

The weight filed are constructed as a field whose influence decays monotonically as distance from the enriching geometry increases. Here, a monotoically decaying Gaussian weight field is chosen

$$w_{\Omega}^{e} = \exp\left(-\frac{d}{d_{\exp}}\right)^{2} w_{\Gamma^{e}} \tag{55}$$

In the spirit of isogeometric analysis, all the aforementioned approximations are carried out using Non-uniform Rational B-Splines, commonly referred to as NURBS surfaces.

7.4 Damage Modeling in ILD stacks

As discussed earlier, the interfaces of the ILD stacks are of nanometers in scale. These interfaces as modeled as material enrichments. The material property of the dielectric are composed with the material property of the crack in the following manner

$$E = (1 - w_{\Omega}^{e})E_0 + w_{\Omega}^{e}E_{in} \tag{56}$$

In the above equation, E is the enriched elastic modulus, E_0 is the modulus of the underlying domain, E_{in} is the modulus of the interface, and w_{Ω}^{e} is the monotonically decaying weight field as shown in Equation(55).

In the enrichment carried out here, the crack was modeled as a discontinuity. However, this assumes the pre-existence of the crack similar to LEFM. Thus, to study the nucleation of cracks, the underlying material modulus was enriched with a damage law as shown below:

$$E = (1 - w_{\Omega}^{e})E_0 + w_{\Omega}^{e}(1 - D)\,\mathrm{E}_0 \tag{57}$$

D is the damage parameter which varies from 0 in an undamaged state to 1. When the material modulus reduces to zero and it can no longer support a load. This could be seen as a special case of Equation (56) where the enriched material modulus of the interface degrades with increase in damage. The damage parameter *D* is defined as follows

$$D = \frac{G}{\Gamma_c} \tag{58}$$

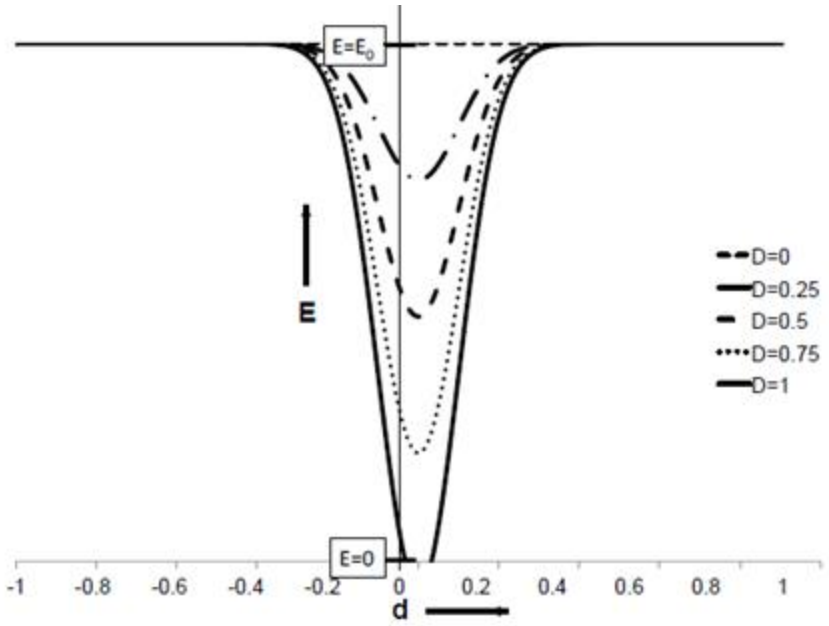

Figure 7-2. Elastic modulus 'decays' on increase in damage parameter [1].

Table 7-1. Cohesive energy density between different material interfaces [1].

Interface	Γ_c (J/m^2)
Sic-Cu	8
ILD-Sic	3
Ta-ILD	5

Where *G* is the energy release rate and Γ_c is the cohesive energy density, which is the area under the cohesive curve. Theoretically, this energy density is the same as interfacial fracture toughness. The influence of damage parameter on the elastic modulus is shown in Figure 7-2 [1]. In cohesive models, there is a cohesive zone ahead of the crack tip, where the two separate cohesive surfaces are held together by the cohesive traction. The separation of the surfaces result in crack propagation, and happens at a critical value of separation displacement at the tail end of the cohesive zone. This critical separation is denoted by δ_c. There exists a wide choice of

cohesive law that describes the relation between the displacement and the traction [65]:

$$\sigma = \sigma_c f\left(\frac{\delta}{\delta_c}\right) \tag{59}$$

In the above relation, σ_c is the peak or critical traction and δ_c is the characteristic displacement. Function *f* describes the shape of the cohesion separation law. There exist several choices of this function in the literature, such as, a linear softening model, bilinear model, trapezoidal model, Dugdale model and exponential model. Trapezoidal model is quite popular, since bilinear model, Dugdale model and the linear softening model are often a special case of the trapezoidal model. These are demonstrated in Figure 7-3.

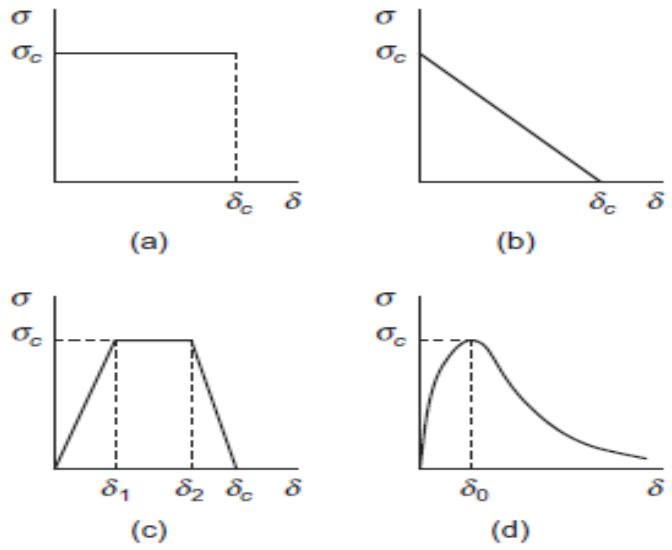

Figure 7-3. (a) Dugdale model(b) Linear cohesive model (c) Trapezoidal model (d) Exponential model [65].

In the present study, a bilinear cohesive model was used in the simulation framework. The bilinear model could be obtained from trapezoidal law when $\delta_1 = \delta_2 = \delta_0$. The damage initiation begins when $\delta = \delta_0$. The cohesive energy density for the bilinear form is given by

$$\Gamma_c = \frac{1}{2}\sigma_c \delta_c \tag{60}$$

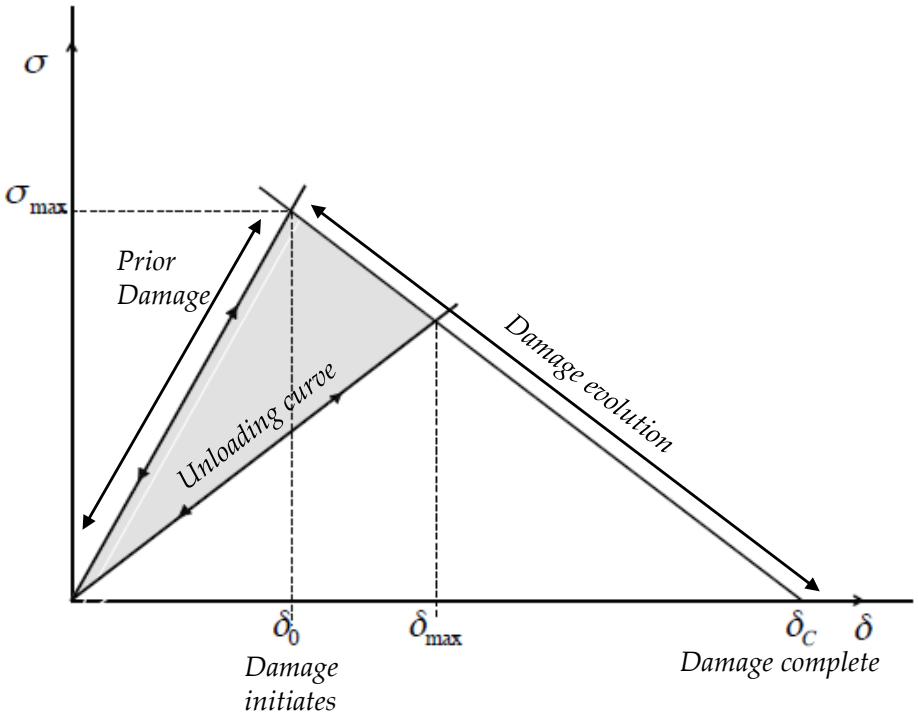

Figure 7-4. Bilinear cohesive damage law to describe material behavior prior and post damage.

7.5 Geometry

In the global wire bonding model, the ILD layer material properties were homogenized due the three orders difference in the length scale between that of the interfaces and the overall structure. The 'macroscale' global model provided the boundary conditions of the 'local' isogeometric model. The local model of the ILD stacks is two dimensional and under the assumption of plane strain conditions. Realistic features such as copper lines and vias have also been included in the local model. The configuration of ILD stacks discussed in reference [1] has been used for the analysis of the wire bonding process. The ILD stacks modeled here are composed of eight metallized layers, denoted by M1-M8. Three different dielectric materials are also included in this stack. Layers M7-M8 are composed of SiO_2, M3-M6 are of ultra

low-k material and M1-M2 layers are composed of SiCOH. Levels M3-M8 contain 34% copper. Material properties from reference [1] were used. Due to very small length scales, the layers M1-M2 were replaced by volume averaged material properties. Material interfaces between the metallized layers were modeled with the properties of etch stop layer made of Sic and barrier layers of Ta.

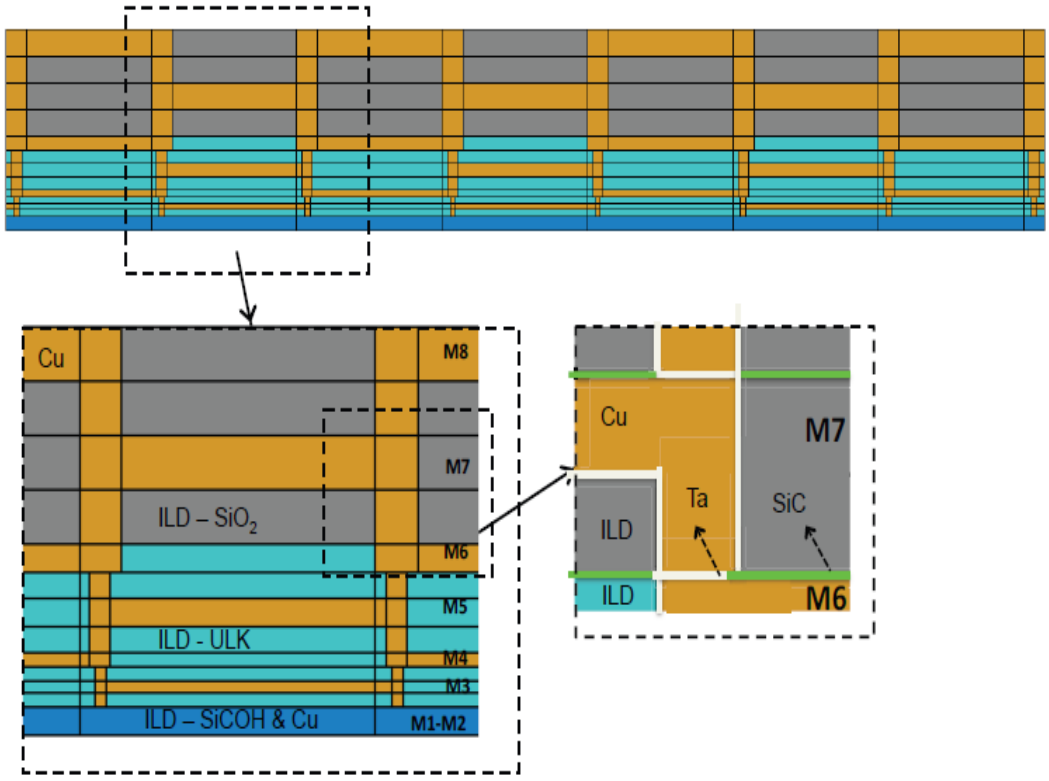

Figure 7-5. A schematic of the analyzed Structure under Pad. The model includes material heterogeneities and features such as etch stops and copper vias [1].

7.6 Boundary Conditions

The critical out-of-plane stresses in the Z-direction was established to be the main driving force for crack nucleation and propagation, as mentioned in the earlier chapter. The deformations U1 and U3 along the four edges of the SUP were converted into appropriate boundary conditions for the local model using spline interpolation functions. The deformations of SUP during the critical stages are shown below in Figure 7-6 and Figure 7-7.

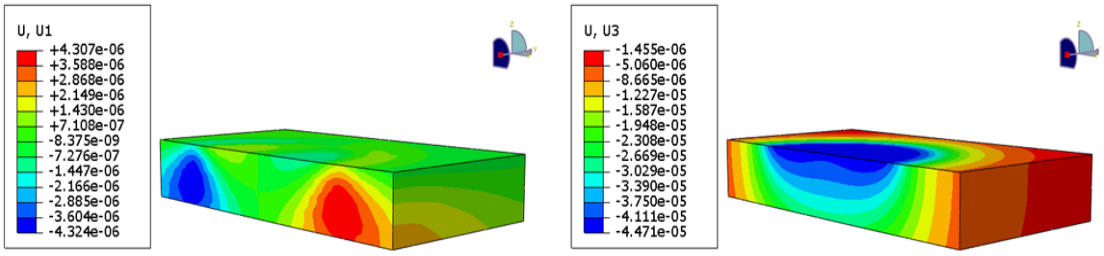

(a) (b)

Figure 7-6. Displacements at the end of impact step, T=1E-6 s.

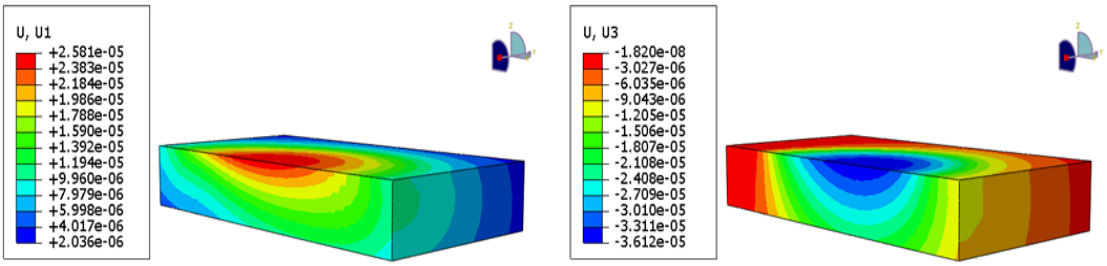

(a) (b)

Figure 7-7. Displacements at the first peak excitation of ultrasonic vibration stage, t=2.5 E-7 s.

These deformations were converted to traction boundary condition for the top face of the local ILD stack model, and as displacement boundary conditions for the other three faces using a spline interpolation function.

7.7 Results and Discussion

The impact and ultrasonic vibration stages were analyzed individually to study the severity of each stage. During the impact stage, the damage is seen to propagate along the vertical interfaces as shown in the Figure 7-8. The maximum value of accumulated damage parameter is 0.1 at the Cu, Ta and ILD-ULK tri-material junctions. During the peak excitation of ultrasonic stage, the horizontal interfaces of M3 and M5 layers were under the risk of delamination as shown in Figure 7-9 and Figure 7-10. These are the interfaces of ILD-ULK material. The maximum accumulated damage were 0.6 and 0.8 at the first and second peak excitations

respectively, during the ultrasonic vibration stage. Thus, it can be concluded that the ultrasonic stage is more severe of the two stages, under given local boundary conditions. The tri-material junctions were the most susceptible to damage.

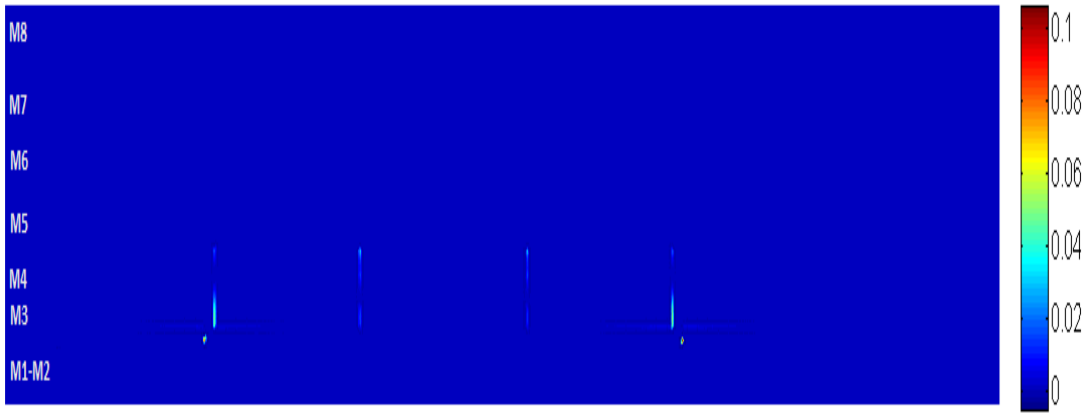

Figure 7-8. Damage accumulated during the end of impact stage, time T=1 E-6 s.

Figure 7-9. Damage accumulated during first peak excitation of ultrasonic stage, t=2.5 E-7 s.

Figure 7-10. Damage accumulated during second peak excitation of ultrasonic stage, t=7.5 E-7 s.

In summary, the limitations of LEFM were discussed, and the theory of enriching the modulus of the underlying material with the cohesive damage law was adopted to simulate crack nucleation as well as crack propagation. Using this simulation framework, the risk of fracture in ULK dies during wire bonding was modeled. The deformations from the global wire bonding model were transferred to the local model as traction boundary conditions on the top face and displacement boundary conditions on the other three faces using spline interpolation functions. The damage accumulation for the critical steps in wire bonding was studied, and the tri-material corner junctions were found to be most susceptible to damage. Other potential sites included the interfaces of the ULK material. It was also concluded that, of the two critical stages of loading, the ultrasonic excitation stage was more severe.

CHAPTER 8. CONCLUSIONS

8.1 Contributions

In this thesis, a multi-scale modeling technique for simulations of fracture in ILD stacks during wire bonding has been proposed. The properties of the Cu free-air ball, which were earlier missing in literature, have been characterized using a custom-built microtester. The microtester contained three linear stages, a tilt stage, two load cells, capacitive stage, Peltier thermocouple and its power source, and a high working-depth lens camera system. Using such an apparatus the micron-scaled FAB of spherical shape was compressed, while enabling a closed loop control using a LabVIEW interface. Compression tests were done at low and intermediate strain rates and at different temperatures. At higher strain rates, it was observed that the forces required to produce the same strain were higher. Thus, a strain hardening effect was deduced. At higher temperatures, the forces required to produce the same amount of strain lowered. Higher temperatures decreased the stiffness of the FAB. These properties were a key component, given the high temperature and high strain rates at which wire bonding processes take place.

Using the properties of copper, elastic contact theories such as Hertz model and Tatara model, and plastic contact theories such as Thornton model were applied to deduce if the theoretical predictions match the observed experimental response, in the absence of which, an analytical method to derive the strain hardening index by substituting Ramberg-Osgood type relation in the contact theories was proposed. The strain-hardening index concluded that the effect of strain hardening gradually reduced at higher strain rates.

A ‘unified’ viscoplastic model was adopted to characterize the material at all strain rates and temperatures. Anand model was chosen for this purpose, having one state variable and tractable number of material parameters. Due to the spherical shape

of the FAB, an inverse procedure was adopted to characterize the material properties. A design space was constructed with an upper and lower limit for each of these variables, and a pattern search optimization algorithm was used to arrive at a set of physically feasible parameters which would explain the observed response at various strain rates. A modified version of Anand model was then enforced to include temperature dependent behavior of the Cu FAB.

Having deduced the material properties of the Cu FAB, a 'global' implicit model of the wire bonding process was constructed. Two of the most severe stages of the wire bonding process, the impact stage and the ultrasonic vibration stage with bonding were simulated. In the impact stage, the FAB was collapsed on the bond pad by a downward motion of capillary, with a velocity of 10 m/s. An ultrasonic displacement of amplitude 1 μm was then applied at a frequency of 100 kHz, for a time period of 1 μs. Important parameters such as contact pressure between FAB and bond pad, and deformation of the FAB, bond pad and the ILD were studied.

The deformations of the edges of SUP in the 'global' finite element model were provided as input to the 'local' isogeometric model of the ILD. This constitutes the final step of muti-scale modeling. The model predicted potential crack initiation sites, and crack propagation path using a damage accumulation parameter. It was concluded that, of the two steps of wire bonding, ultrasonic step causes greater damage.

8.2 Future Work

The multi-scale simulation frame work is an essential step towards the design of crack arrest features in the chips.

LIST OF REFERENCES

LIST OF REFERENCES

[1] K. Upreti, G. Subbarayan, D. Y. Jung, and B. Sammakia, "Simulations of damage and fracture in ULK under pad structures during Cu wirebond process," *Fourteenth Intersoc. Conf. Therm. Thermomechanical Phenom. Electron. Syst.*, pp. 609–615, May 2014.

[2] H. Lin, K. Upreti, A. Tippmann, G. Subbarayan, D. Y. Jung, and B. Sammakia, "Simulations of Deformation and Stress During Copper Wirebond on ULK Chips," in *Volume 1: Advanced Packaging; Emerging Technologies; Modeling and Simulation; Multi-Physics Based Reliability; MEMS and NEMS; Materials and Processes*, 2013, p. V001T04A012.

[3] B. Nachon, "Basics of Ball Bonding."

[4] S. K. Prasad, *Advanced Wirebond Interconnection Technology*. .

[5] C. J. Hang, C. Q. Wang, Y. H. Tian, M. Mayer, and Y. Zhou, "Microstructural study of copper free air balls in thermosonic wire bonding," *Microelectron. Eng.*, vol. 85, no. 8, pp. 1815–1819, Aug. 2008.

[6] T. Gupta, *Copper Interconnect Technology*. New York, NY: Springer New York, 2009.

[7] C. T. Lu, "The challenges of copper wire bonding," in *2010 5th International Microsystems Packaging Assembly and Circuits Technology Conference*, 2010, pp. 1–4.

[8] T. Gupta, *Copper Interconnect Technology*. .

[9] M. Rasco, K. Mosig, J. L. J. Ling, P. Elenius, and R. Augur, "Packaging assessment of porous ultra low-k materials," *Proc. IEEE 2002 Int. Interconnect Technol. Conf. (Cat. No.02EX519)*, 2002.

[10] B. Chylak, "Wafer Probe , Wire Bond , and Packaging Issues for Low K Dielectric Materials," *Technology*, 2002.

[11] P. Liu, L. Tong, J. Wang, L. Shi, and H. Tang, “Challenges and developments of copper wire bonding technology,” *Microelectron. Reliab.*, vol. 52, no. 6, pp. 1092–1098, Jun. 2012.

[12] H. Lin, “Configurational optimization for optimal topological and fracture-resistant designs of solids,” 2014.

[13] G. Lorenz, M. Petzold, M. Mittag, C. Dresbach, and E. Milke, “Mechanical characterization of gold and copper free air balls in thermosonic wire bond interconnections,” in *Electronics System Integration Technology Conference, ESTC 2010 - Proceedings*, 2010.

[14] C. J. Hang, W. H. Song, I. Lum, M. Mayer, Y. Zhou, C. Q. Wang, J. T. Moon, and J. Persic, “Effect of electronic flame off parameters on copper bonding wire: Free-air ball deformability, heat affected zone length, heat affected zone breaking force,” *Microelectron. Eng.*, vol. 86, no. 10, pp. 2094–2103, Oct. 2009.

[15] R. Guo, L. Gao, D. Mao, M. Li, X. Wang, Z. Lv, and H. Chiu, “Study of free air ball formation in Ag–8Au–3Pd alloy wire bonding,” *Microelectron. Reliab.*, vol. 54, no. 11, pp. 2550–2554, Nov. 2014.

[16] S. S. Paranjothy, “Characterization of cu free air ball constitutive behavior using microscale compression test,” in *Fourteenth Intersociety Conference on Thermal and Thermomechanical Phenomena in Electronic Systems (ITherm)*, 2014, pp. 365–368.

[17] A. Tambat, H.-Y. Lin, G. Subbarayan, D. Y. Jung, and B. Sammakia, “Simulations of Damage, Crack Initiation, and Propagation in Interlayer Dielectric Structures: Understanding Assembly-Induced Fracture in Dies,” *IEEE Trans. Device Mater. Reliab.*, vol. 12, no. 2, pp. 241–254, Jun. 2012.

[18] A. Tambat and G. Subbarayan, “Isogeometric enriched field approximations,” *Comput. Methods Appl. Mech. Eng.*, vol. 245–246, pp. 1–21, 2012.

[19] D. K. Chan, “A maximum entropy fracture model for low and high strain-rate fracture in TinSilverCopper alloys.,” Purdue University, 2012.

[20] P. S. Follansbee and U. F. Kocks, “A constitutive description of the deformation of copper based on the use of the mechanical threshold stress as an internal state variable,” *Acta Metall.*, vol. 36, no. 1, pp. 81–93, Jan. 1988.

[21] T. Glenn and W. Bradley, “The Origin of Strain-Rate Sensitivity in OFHC Copper,” *Metall. Trans.*, vol. 4, no. October, p. pp 2343–2348, 1973.

[22] S. . Bordner and A. Merzer, “Viscoplastic Constitutive Equations for Copper with Strain Rate History and Temperature Effects,” *J. Eng. Mater. Technol.*, pp. 388–394.

[23] K. L. Johnson, *Contact Mechanics*, vol. 37. 1985, pp. 1–17.

[24] Y. Tatara, “On Compression of Rubber Elastic Sphere Over a Large Range of Displacements—Part 1: Theoretical Study,” *J. Eng. Mater. Technol.*, vol. 113, no. 3, p. 285, 1991.

[25] Y. Tatara, S. Shima, and J. C. Lucero, “On Compression of Rubber Elastic Sphere Over a Large Range of Displacements—Part 2: Comparison of Theory and Experiment,” *J. Eng. Mater. Technol.*, vol. 113, no. 3, p. 292, 1991.

[26] L.-Y. Li, C. Thornton, and C.-Y. Wu, “Impact behaviour of elastoplastic spheres with a rigid wall,” *Proc. Inst. Mech. Eng. Part C J. Mech. Eng. Sci.*, vol. 214, no. 8, pp. 1107–1114, Jan. 2000.

[27] C. Thornton, “Coefficient of Restitution for Collinear Collisions of Elastic-Perfectly Plastic Spheres,” *J. Appl. Mech.*, vol. 64, no. 2, p. 383, 1997.

[28] J. Lubliner, *Plasticity Theory*. .

[29] U. F. Kocks, A. . Argon, and M. F. Ashby, *Thermodynamics and Kinetics of Slip: Vol.19*. 1975, pp. 231–234.

[30] J. Lubliner and B. Moran, “Plasticity Theory,” *Journal of Applied Mechanics*, vol. 59. p. 245, 1992.

[31] D. L. McDowell, “A nonlinear kinematic hardening theory for cyclic thermoplasticity and thermoviscoplasticity,” *Int. J. Plast.*, vol. 8, no. 6, pp. 695–728, Jan. 1992.

[32] J. Moosbrugger, “A rate-dependent bounding surface model with a generalized image point for cyclic nonproportional viscoplasticity,” *J. Mech. Phys. Solids*, vol. 38, no. 5, pp. 627–656, 1990.

[33] H. Ishikawa, “Subsequent yield surface probed from its current center,” *Int. J. Plast.*, vol. 13, no. 6–7, pp. 533–549, Jan. 1997.

[34] E. W. Hart, “Constitutive Relations for the Nonelastic Deformation of Metals,” *J. Eng. Mater. Technol.*, vol. 98, no. 3, p. 193, 1976.

[35] E. P. Busso, M. Kitano, and T. Kumazawa, "Modeling Complex Inelastic Deformation Processes in IC Packages' Solder Joints," *J. Electron. Packag.*, vol. 116, no. 1, p. 6, 1994.

[36] E. P. Busso, M. Kitano, and T. Kumazawa, "A Visco-Plastic Constitutive Model for 60/40 Tin-Lead Solder Used in IC Package Joints," *J. Eng. Mater. Technol.*, vol. 114, no. 3, p. 331, 1992.

[37] Y. Tachibana and E. Krempl, "Modeling of High Homologous Temperature Deformation Behavior Using the Viscoplasticity Theory Based on Overstress (VBO): Part I— Creep and Tensile Behavior," *J. Eng. Mater. Technol.*, vol. 117, no. 4, p. 456, 1995.

[38] Y. Tachibana and E. Krempl, "Modeling of High Homologous Temperature Deformation Behavior Using the Viscoplasticity Theory Based on Overstress (VBO): Part II—Characteristics of the VBO Model," *J. Eng. Mater. Technol.*, vol. 119, no. 1, p. 1, 1997.

[39] Y. Tachibana and E. Krempl, "Modeling of High Homologous Temperature Deformation Behaviour Using the Viscoplasticity Theory Based on Overstress (VBO): Part III—A Simplified Model," *J. Eng. Mater. Technol.*, vol. 120, no. 3, p. 193, 1998.

[40] L. Anand, "Constitutive Equations for the Rate-Dependent Deformation of Metals at Elevated Temperatures," *J. Eng. Mater. Technol.*, vol. 104, no. 1, p. 12, 1982.

[41] G. Z. Wang, Z. N. Cheng, K. Becker, and J. Wilde, "Applying Anand Model to Represent the Viscoplastic Deformation Behavior of Solder Alloys," *J. Electron. Packag.*, vol. 123, no. 3, p. 247, 2001.

[42] S. Koric and B. G. Thomas, "Thermo-mechanical models of steel solidification based on two elastic visco-plastic constitutive laws," *J. Mater. Process. Technol.*, vol. 197, no. 1–3, pp. 408–418, Feb. 2008.

[43] ANSYS Inc., "ANSYS Documentation." ANSYS Inc, 2007.

[44] S. R. Kalidindi and L. Anand, "Large deformation simple compression of a copper single crystal," *Metall. Trans. A*, vol. 24, no. 4, pp. 989–992, Apr. 1993.

[45] D. Chan, X. Nie, D. Bhate, G. Subbarayan, W. W. Chen, and I. Dutta, "Constitutive Models for Intermediate- and High-Strain Rate Flow Behavior of Sn3.8Ag0.7Cu and Sn1.0Ag0.5Cu Solder Alloys," *IEEE Trans. Components, Packag. Manuf. Technol.*, vol. 3, no. 1, pp. 133–146, Jan. 2013.

[46] R. Hooke and T. A. Jeeves, "`` Direct Search'' Solution of Numerical and Statistical Problems," *J. ACM*, vol. 8, no. 2, pp. 212–229, Apr. 1961.

[47] V. Sulimov, P. Shkapov, and S. Nosachev, "Hooke–Jeeves Method-used Local Search in a Hybrid Global Optimization Algorithm," *Sci. Educ. Bauman MSTU*, vol. 14, no. 06, Jun. 2014.

[48] K. Prasada, C. Rao, and D. Rao, "Optimizing pulsed current micro plasma arc welding parameters to maximize ultimate tensile strength of Inconel625 Nickel alloy using response surface method," *International Journal of Engineering, Science and Technology*, vol. 3, no. 6. 2012.

[49] D. Szeliga, J. Gawąd, and M. Pietrzyk, "Parameters identification of material models based on the inverse analysis," *Int. J. Appl. Math. Comput. Sci.*, vol. 14, no. 4, pp. 549–556.

[50] N. Bai, X. Chen, and H. Gao, "Simulation of uniaxial tensile properties for lead-free solders with modified Anand model," *Mater. Des.*, vol. 30, no. 1, pp. 122–128, Jan. 2009.

[51] W. Qiang, L. Lihua, C. Xuefan, W. Xiaohong, Y. Liu, S. Irving, and T. Luk, "Experimental Determination and Modification of Anand Model Constants for Pb-Free Material 95.5Sn4.0Ag0.5Cu," in *2007 International Conference on Thermal, Mechanical and Multi-Physics Simulation Experiments in Microelectronics and Micro-Systems. EuroSime 2007*, 2007, pp. 1–9.

[52] M. Sakane, "Modified Anand constitutive model for lead-free solder Sn-3.5Ag," in *The Ninth Intersociety Conference on Thermal and Thermomechanical Phenomena In Electronic Systems (IEEE Cat. No.04CH37543)*, 2004, pp. 447–452.

[53] M. Sakane, "Modified Anand constitutive model for lead-free solder Sn-3.5Ag," in *The Ninth Intersociety Conference on Thermal and Thermomechanical Phenomena In Electronic Systems (IEEE Cat. No.04CH37543)*, pp. 447–452.

[54] C. Dresbach, G. Lorenz, M. Petzold, and H. Altenbach, "Analysis of Chip Damage Risk in Thermosonic Wire Bonding," *Key Eng. Mater.*, vol. 478, pp. 75–80, Apr. 2011.

[55] Dassault Systèmes, "Abaqus Documentation," *Dassault Systèmes*. Dassault Systèmes, 2013.

[56] C.-L. Yeh and Y.-S. Lai, "Transient analysis of the impact stage of wirebonding on Cu/low-K wafers," *Microelectron. Reliab.*, vol. 45, no. 2, pp. 371–378, Feb. 2005.

[57] M. Su and F. Kuechenmeister, “Chip package interaction (CPI) reliability of Cu/low-k/ultra-low-k interconnect,” in *2009 16th IEEE International Symposium on the Physical and Failure Analysis of Integrated Circuits*, 2009, pp. 691–693.

[58] I. Ocana, J. Molinaaldareguia, D. Gonzalez, M. Elizalde, J. Sanchez, J. Martinezesnaola, J. Gilsevillano, T. Scherban, D. Pantuso, and B. Sun, “Fracture characterization in patterned thin films by cross-sectional nanoindentation☆,” *Acta Mater.*, vol. 54, no. 13, pp. 3453–3462, Aug. 2006.

[59] M. Stolarska and D. L. Chopp, “Modeling thermal fatigue cracking in integrated circuits by level sets and the extended finite element method,” *Int. J. Eng. Sci.*, vol. 41, no. 20, pp. 2381–2410, Dec. 2003.

[60] J. M. Melenk and I. Babuška, “The partition of unity finite element method: Basic theory and applications,” *Comput. Methods Appl. Mech. Eng.*, vol. 139, no. 1–4, pp. 289–314, Dec. 1996.

[61] I. Babuška and J. M. Melenk, “The Partition of Unity Method,” *Int. J. Numer. Methods Eng.*, vol. 40, no. 4, pp. 727–758, Feb. 1997.

[62] T. Strouboulis, I. Babuška, and K. Copps, “The design and analysis of the Generalized Finite Element Method,” *Comput. Methods Appl. Mech. Eng.*, vol. 181, no. 1–3, pp. 43–69, Jan. 2000.

[63] T. Strouboulis, K. Copps, and I. Babuška, “The generalized finite element method,” *Comput. Methods Appl. Mech. Eng.*, vol. 190, no. 32–33, pp. 4081–4193, May 2001.

[64] J. Dolbow, N. Moës, and T. Belytschko, “Discontinuous enrichment in finite elements with a partition of unity method,” *Finite Elem. Anal. Des.*, vol. 36, no. 3–4, pp. 235–260, Nov. 2000.

[65] C. Sun and Z. Jin, “Fracture Mechanics.”